Research Square

Preprints are preliminary reports that have not undergone peer review.
They should not be considered conclusive, used to inform clinical practice,
or referenced by the media as validated information.

Selective survival at the Cretaceous–Paleogene boundary driven by infrared radiation and climate cooling

Kunio Kaiho

kunio.kaiho.a6@tohoku.ac.jp

Tohoku University

Naga Oshima

Meteorological Research Institute

Tatsuro Ando

Ashoro Museum of Paleontology

Article

Keywords: birds, Cretaceous-Paleogene boundary, crocodilians, dinosaurs, mammals, mass extinction, migration, primary productivity, survival

Posted Date: July 3rd, 2026

DOI: https://doi.org/10.21203/rs.3.rs-10072735/v1

License: This work is licensed under a Creative Commons Attribution 4.0 International License. Read Full License

Additional Declarations: No competing interests reported.

Abstract

The extinction and survival mechanisms of terrestrial animals at the Cretaceous–Paleogene (K–Pg) boundary remain poorly resolved. Here we reconstruct global paleoclimate classifications, terrestrial net primary productivity, and the distributions of non-avian dinosaurs, birds, crocodilians, and mammals across the Chicxulub impact using an asteroid-impact scenario. Our results indicate that intense infrared radiation from reentering ejecta immediately after the impact caused severe mortality among unsheltered tetrapods, including non-avian dinosaurs. During the subsequent 1–3 years, cold desert, tundra, and ice-cap climates expanded across most land areas, with appearance of only limited temperate refugia. These refugia explain differential survival and post-impact migration patterns among the four animal groups. Comparisons between model-derived refuges and fossil-based Danian habitable areas enable reconstruction of survival migration routes for birds, crocodilians, and mammals. Our findings highlight the critical roles of infrared radiation and short-term climatic cooling in shaping selective survival at the K–Pg boundary.

Introduction

The Cretaceous–Paleogene (K–Pg) mass extinction was triggered by the impact of a large asteroid onto the low-latitude continental shelf of the Yucatán Peninsula, Mexico[1–3]. Recent studies indicate that dinosaur diversity showed little evidence of a long-term global decline prior to the extinction event[4]. Contemporaneous Deccan Traps volcanism may have contributed to environmental stress, as elevated mercury (Hg) concentrations occur near the extinction horizon[5,6]. However, mercury isotope data (δ^{202}Hg and Δ^{199}Hg) from three geographically distant K–Pg boundary sections converge only within the iridium (Ir)-enriched impact layer and immediately below it, suggesting that much of the Hg was derived from impact-target rocks and subsequently dispersed on a global scale[6].

The Chicxulub impact generated intense thermal radiation through atmospheric re-entry of ejecta, exposing Earth's surface to severe infrared heating[7–9]. In addition, the impact injected large quantities of soot, sulfur-bearing gases, dust, mercury, and halogen compounds into the atmosphere, causing rapid and profound environmental perturbations, including global darkness, cooling, reduced precipitation, acid rain, and ozone depletion[6,10–14]. Climate-model simulations and geochemical evidence indicate that the asteroid impact, rather than Deccan volcanism, was the primary driver of the end-Cretaceous mass extinction[6,15].

Despite the collapse of terrestrial and marine ecosystems, several vertebrate groups—including birds, mammals, crocodilians, turtles, lizards, and snakes—survived the crisis[16–19]. The mechanisms responsible for this selective survival remain incompletely understood[1,16,20]. Infrared radiation likely caused high mortality among large, surface-dwelling vertebrates lacking access to shelter[7–9], whereas prolonged cooling and reduced net primary productivity (NPP) disrupted food webs and severely affected organisms dependent on plant-based energy pathways[11,16,21] (Supplementary Fig. 1). Many surviving vertebrates may have benefited from ecological buffering provided by underground refuges or aquatic habitats[16–18]. Crocodilians, for example, occupied semi-aquatic environments and could exploit detritus-based food webs, potentially reducing their vulnerability to ecosystem collapse. Surviving birds may also have possessed ecological traits that enhanced persistence under post-impact conditions[20,22], although the processes underlying avian survival remain poorly resolved.

A major obstacle to understanding survival mechanisms is the absence of a fossil record spanning the approximately 15-year interval between the Chicxulub impact and subsequent climate recovery. Consequently, fossil data alone cannot directly reveal how terrestrial vertebrates survived or became extinct during this critical period. To address this gap, we combined climate and ecosystem simulations covering the first 15 years after the impact with global fossil-distribution data. Our primary objective is to reconstruct survival strategies immediately following the impact and to identify potential refugial habitats that cannot be inferred from fossils alone. By comparing model-derived habitable regions with Maastrichtian and Danian fossil distributions, we evaluate survival and dispersal pathways for major terrestrial tetrapod groups and reconstruct the broader faunal and biogeographic changes that occurred across the K–Pg boundary. Our results suggest that mammals and crocodilians survived primarily through sheltering behaviours, whereas birds, and possibly some crocodilian populations, additionally relied on migration to climatic refugia.

Results and Discussion

Survival-extinction patterns of tetrapod vertebrates from fossil records

To characterize survival and extinction patterns across the K–Pg boundary, we analyzed four representative tetrapod groups: non-avian dinosaurs, birds, crocodilians, and mammals (Fig. 1). Non-avian dinosaurs became extinct, whereas birds, crocodilians, and mammals survived with varying degrees of success. Species richness and genus richness exhibit similar patterns across the K–Pg boundary in birds, crocodilians, and mammals (Fig. 1i–l).

Bird diversity declined sharply across the boundary, although ground-dwelling neornithine birds survived while arboreal forms disappeared (Fig. 1c, d)[20]. Despite their low abundance in the earliest Danian fossil record, birds subsequently underwent the most rapid diversification among

surviving tetrapods, becoming a dominant component of Cenozoic terrestrial vertebrate faunas (Fig. 1j).

Crocodilians experienced substantial extinction but retained several surviving lineages and rapidly re-expanded during the Danian (Fig. 1e, f). Mammals also survived globally and underwent major taxonomic restructuring across the boundary, with eutherian mammals becoming increasingly dominant in the Danian (Fig. 1g, h). Mammalian diversity increased substantially during the early Paleogene (Fig. 1l).

Although fossil data document the long-term consequences of the extinction event, they provide limited information on survival during the short-lived impact winter immediately following the Chicxulub impact. To investigate the mechanisms underlying survival and extinction, we reconstructed post-impact climate and terrestrial net primary productivity (NPP) using climate–ecological simulations (Figs. 2–7). These results were integrated with global fossil-distribution data to identify potential refugia, survival regions, and migration pathways across the K–Pg boundary (Fig. 6). Further details are provided in the Supplementary Information (Detailed Text 1).

Characteristics of four tetrapod groups for survival strategy

The four tetrapod groups examined in this study differed markedly in ecological traits that likely influenced survival across the K–Pg boundary (Fig. 1; Supplementary Table 1). Non-avian dinosaurs generally had relatively large body sizes, limited access to shelter, and low tolerance of near-surface cold conditions[1,16]. Birds were typically smaller-bodied, capable of sheltering, able to fly, and more tolerant of cooler climatic conditions. Both groups were strongly dependent on plant-based food chains and therefore vulnerable to reductions in terrestrial net primary productivity (NPP).

In contrast, crocodilians and mammals were more closely associated with sheltered habitats and detritus-based food webs, factors that likely increased survival potential relative to non-avian dinosaurs and birds. Crocodilians, however, appear to have been less tolerant of low temperatures than mammals, which may explain their lower survival rate. Although mammals exhibited the highest survival among the four groups, only a small fraction of mammalian species persisted across the K–Pg boundary, indicating that environmental stress remained severe even for the most resilient terrestrial vertebrates[18,23].

Body size was another important factor influencing survival. Non-avian dinosaurs generally required substantially greater food resources than birds and were therefore more vulnerable to the collapse of primary productivity. In contrast, the small body size of surviving birds reduced energetic demands and likely enhanced their ability to persist under resource-limited conditions. Fossil evidence further suggests that ornithurines, including surviving neornithines, possessed flight capabilities comparable to those of modern birds and potentially superior to those of extinct enantiornithines (Supplementary Information, Detailed Text 2; Supplementary Fig. 2)[24–28]. The combination of small body size, low food requirements, and advanced flight performance may have facilitated access to scattered refugial habitats and contributed to the selective survival and subsequent diversification of crown birds following the K–Pg extinction.

Environmental disturbance before impact winter

Immediately after the asteroid impact, intense infrared radiation, heat pulses, wildfires, ozone depletion, acid rain, and underwater shock waves caused severe but likely incomplete ecosystem collapse[7, 8, 29, 30] (Fig. 2). Many exposed terrestrial organisms suffered heavy mortality, although survival was possible in open habitats, underground refuges, aquatic environments, or sparsely vegetated regions. Temporary food shortages following wildfire destruction and reduced plant productivity further stressed herbivores and higher trophic levels. Birds may have benefited from small body size and flight capability, mammals from burrowing behavior and flexible diets, and crocodilians from aquatic refuges. While these short-term disturbances caused major population declines, prolonged global cooling and reduced sunlight during the subsequent impact winter were likely the primary drivers of mass extinction (Fig. 2). Further details are provided in the Supplementary Information (Detailed Text 3).

Climate changes after the Chicxulub impact

To investigate regional-scale climatic changes following the Chicxulub impact and identify potential refugia for terrestrial animals, we applied high-resolution modern climate-model simulations, as equivalent simulations are not yet available for end-Cretaceous boundary conditions. We reconstructed Köppen climate classification maps for four intervals: pre-impact, the first post-impact year, the coldest year, and the mid-recovery phase (Supplementary Figs. 3 and 4; Supplementary Tables 3 and 4). Supplementary Figures 4a–j present enlarged regional views from Supplementary Figure 3, highlighting the emergence of transient temperate regions after the impact. These maps illustrate changes in climate classification driven by shifts in surface air temperature and precipitation under the soot-emission scenario in representative regions of Europe–Africa, Australia–the Maritime Continent, and southern North America.

The simulations indicate that narrow temperate zones developed along the western margins of subtropical deserts and within low-latitude oceanic climate regions, whereas many pre-impact temperate and tropical regions shifted to tundra and cold-desert climates owing to severe cooling and reduced precipitation caused by diminished solar radiation (Supplementary Figs. 4a–j). Southern Europe–northwestern Africa was selected as a representative region because its paleogeographic setting closely resembles both modern geography and the end-Cretaceous

configuration. Likewise, present-day Australia, characterized by extensive deserts, serves as a useful analogue for southwestern South America at comparable Southern Hemisphere latitudes during the K–Pg interval.

To generate post-impact end-Cretaceous climate maps, we translated modern climate-model results into end-Cretaceous conditions using the relationships summarized in Supplementary Tables 3 and 4. These tables document transitions between pre-impact and post-impact climate types under soot and SO_2 scenarios during the first year, coldest year, and recovery stage. We then applied these transitions to the end-Cretaceous climate classification map of Burgener et al.[31], including modifications for low-latitude oceanic regions that shifted from tropical to warm-temperate climates (Supplementary Table 3; Supplementary Fig. 4b, c, f, g, j). This procedure enabled reconstruction of post-impact climate classification maps (Fig. 2).

From the pre-impact interval to the coldest phase, mid-latitude regions (30°–60°) shifted from temperate to tundra climates, whereas many tropical and subtropical regions transformed into extensive cold deserts. In contrast, transient temperate climates appeared along the western margins of former hot deserts in northwestern Africa, western Asia, and western-central South America (15°–30° in both hemispheres), as well as in low-latitude oceanic regions, and persisted for several years in both soot and SO_2 scenarios (Fig. 2b, c, e, f).

The development of these transient temperate zones is attributed to weakening and equatorward contraction of the Hadley circulation following the impact (Fig. 2h–k, Supplementary Fig. 7). The equatorward migration of the subtropical westerly jet increased precipitation and soil moisture by redirecting migratory cyclonic systems into subtropical desert margins. These anomalous climate patterns gradually weakened during the recovery phase. Additional details are provided in the Supplementary Information.

Results from other climate scenarios

Senel et al.[12] reported global mean surface temperature anomalies of approximately 8 °C cooling for soot, 11 °C cooling for silicate dust, 20 °C cooling for sulfur aerosols, and 15 °C cooling for combined aerosol scenarios. In comparison, our scenario indicates intermediate surface temperature anomalies of approximately 12 °C cooling for soot[32] and 12 °C cooling for sulfur aerosols (Supplementary Figs. 8 and 9). The combined aerosol scenario of Senel et al.[12], with a global cooling of 15 °C, is therefore ~3 °C cooler than the 12 °C cooling obtained in our soot scenario[32].

Temperature anomalies in low-latitude regions closely track the global mean anomalies. A further ~3 °C reduction in low-latitude temperatures, as suggested by the combined aerosol scenario of Senel et al.[12], would likely render conditions unsuitable for crocodilians, consistent with the survival thresholds summarized in crocodilian distribution section (Supplementary Table 5). This discrepancy may be due to their no consideration of high SO_3 emission rate (~97%)[32] for their model, because most of SO_3 change to sulfuric acid aerosols (H_2SO_4 +H_2O) in the impact cloud leading to coagulation with dust leading to fallout and removal from the atmosphere[33]. 20 °C cooling by sulfur aerosols can be overestimate.

Relationship between climate classifications and fossil occurrences

Because fossil distributions immediately after the asteroid impact cannot be directly observed, we examine the relationship between climate classifications before the impact and after recovery, and the fossil occurrences of non-avian dinosaurs, birds, crocodilians, and mammals during the Maastrichtian and Danian ages (Supplementary Table 6). Non-avian dinosaurs are recorded from tropical, temperate, and cold climate zones during the Maastrichtian. Birds are found exclusively in temperate climates during both the Maastrichtian and the Danian. Crocodilians occur in tropical and temperate climates during both intervals, except in the coolest temperate regions. Mammals occupied primarily tropical and temperate climates during the Maastrichtian and Danian, with only a single occurrence in a cold climate during the Maastrichtian. The climate classification maps reconstructed for each animal group before the impact and after recovery are consistent with their respective fossil distributions (Supplementary Table 6).

Terrestrial plant productivity after the asteroid impact

Terrestrial primary productivity declined immediately after the asteroid impact due to global infrared radiation and widespread wildfires, which greatly reduced leaf area and photosynthetic surface coverage, particularly in forests and grasslands (Fig. 3a, b). In contrast, pre-impact subtropical desert regions experienced little direct wildfire damage because of their sparse vegetation cover.

We reconstructed terrestrial net primary productivity (NPP) distributions for the pre-impact interval and for several days, as well as the first, third, and sixth years after the impact. The calculations incorporated temperature, precipitation, sunlight reduction, and NPP loss caused by infrared radiation and wildfires. Analyses focused mainly on low-latitude regions (0°–30°), where climate zones differed only modestly from those of the latest Cretaceous (Supplementary Table 7).

Immediately after the impact, NPP decreased globally to <0.11 kg C m^{-2} yr^{-1} owing to severe sunlight reduction caused by stratospheric soot and aerosols (Fig. 3b). During the first month, solar radiation declined to only 5–10% of pre-impact levels (Supplementary Fig. 6a, b), resulting in substantial suppression of photosynthesis. Model results indicate that low-latitude NPP declined to approximately 30–34% of pre-impact values. Nevertheless, limited vegetation survived in subtropical desert regions and tropical to temperate oceanic climate zones, many of which were island environments. These refugia appeared during the first year after the impact and persisted until approximately the third year, with minimum NPP occurring during the second year. Together, these areas represented only ~0.5% of global land area.

Vegetation recovery gradually expanded after the third year. Regions with NPP >0.14 kg C m^{-2} yr^{-1} increased progressively, reaching ~50% of pre-impact productivity by the sixth year, particularly in low- and mid-latitude regions. Full recovery of terrestrial NPP likely required more than 15 years (Supplementary Fig. 3).

Habitable areas of non-avian dinosaurs and birds

Non-avian dinosaurs and pterosaurs were highly vulnerable to global infrared radiation generated by ejecta re-entry, except for individuals sheltered in caves or other protected environments. This intense heat pulse likely caused severe mortality among exposed terrestrial vertebrates. Dinosaurs, including birds, depended on primary productivity–based food webs, and their potential post-impact distributions were reconstructed using terrestrial net primary productivity (NPP) maps (Fig. 4; Supplementary Table 8). Habitable areas were defined as regions with NPP values exceeding 0.14 kg C m^{-2} yr^{-1}, corresponding to productivity levels comparable to cold deciduous forests and higher than typical tundra environments (Fig. 4)[34].

A major ecological difference between birds and non-avian dinosaurs was flight capability. Birds required less food because of their smaller body size and lower energetic demands[24, 25, 35]. Flight would have enabled birds to locate surviving vegetation and refugia over large distances, providing a major survival advantage during the post-impact environmental crisis. Consequently, reconstructed bird distributions closely matched the limited vegetation refugia identified in the climate simulations (Figs. 2b, c, e, f, 3c, d), although habitable areas contracted to only ~0.65% of global land area during the interval of minimum NPP.

The surviving vegetated regions formed isolated, island-like patches after the impact. Previous studies have shown strong relationships between island area, dispersal ability, and vertebrate diversity[36]. Applying these relationships, non-avian dinosaurs likely behaved ecologically like birds with low dispersal ability and would have struggled to colonize the newly formed fragmented refugia. In contrast, volant birds with high dispersal ability could more effectively occupy these isolated habitats.

During the first four years after the impact, sunlight remained severely reduced, averaging ~5% of pre-impact levels in the first year, ~10% in the second year, and ~22–25% in the third to fourth years. Although temperatures and precipitation generally remained within ranges permitting vegetation survival, low sunlight strongly limited plant productivity. Habitable areas became increasingly restricted to isolated temperate refugia, mainly in regions corresponding to former subtropical deserts. Under these conditions, only vertebrates capable of long-distance dispersal and independent of forest ecosystems were likely to maintain viable populations. Among terrestrial dinosaurs, this ecological profile was characteristic only of some ground-dwelling birds.

Population estimates based on habitable area and body size indicate that approximately 30,000–200,000 birds could have survived within refugial regions, allowing the persistence of multiple species (Table 1, Supplementary Table 9). In contrast, only approximately 200–1,000 non-avian dinosaurs could have survived, suggesting that their populations may have fallen below thresholds required for long-term viability. According to the Allee effect and the 50/500 rule, a minimum census population of roughly 250–500 individuals is generally required to avoid short-term inbreeding depression, whereas 2,500–5,000 individuals may be necessary to maintain long-term genetic diversity[37–39]. In addition, reproductive success in many large vertebrates is often highly skewed, with a small number of dominant males contributing disproportionately to reproduction. Such reproductive skew reduces the effective population size relative to the census population, thereby increasing the number of individuals required to sustain genetically viable populations over evolutionary timescales. These considerations suggest that non-avian dinosaur populations surviving within refugial regions were unlikely to have remained demographically and genetically viable, ultimately leading to extinction.

Field et al.[20] proposed that K–Pg forest collapse filtered out tree-dwelling flying dinosaurs, leaving predominantly non-arboreal neornithines that later diversified rapidly into modern bird ecologies. Consistent with this view, the refugial regions that developed in pre-impact deserts during the first few years after the asteroid impact were probably largely treeless, favouring non-arboreal birds while disadvantaging arboreal taxa. Together with their small body size and efficient flight capabilities, these conditions may have promoted the selective survival and rapid post-impact recovery of crown birds.

Habitable areas of crocodilians

Crocodilians spend much of their time in water and were therefore relatively sheltered from intense infrared radiation and wildfires following the impact. This ecological refuge likely contributed to their survival and indicates that these factors alone cannot fully account for the comparatively low survival rate of crocodilians.

Modern crocodilians, including American and Chinese alligators, are capable of brumation during winter. Their present-day distribution suggests that crocodilian activity requires warmest-month temperatures exceeding ~16 °C (typically >19 °C), while survival is limited by coldest-month temperatures of approximately 5.5 °C (Markwick, 1998). This lower thermal threshold corresponds to the central portion of the Cb climate zone in the Maastrichtian global climate classification map of Burgener et al.[31] (Fig.2a). This interpretation is consistent with fossil evidence for the northernmost extent of crocodilian distributions during the Maastrichtian and Danian (Fig. 6e, f).

After the Chicxulub impact, crocodilian survival was constrained to regions within a narrow annual habitable temperature range, corresponding to low-latitude areas that covered only ~3.2% of the global land surface (Fig. 5c), based on Table 1 and Supplementary Table 10.

Habitable areas of mammals

Late Cretaceous small mammals likely spent much of their time underground, similar to many modern rodents, enabling them to avoid predators and environmental hazards. This behavior would also have provided effective protection from the intense infrared radiation and widespread wildfires triggered by the asteroid impact. Their subterranean lifestyle further buffered them against the prolonged global cooling that followed, allowing mammals to tolerate both the immediate impact effects and the subsequent climatic deterioration.

Fossil distributions indicate that mammals generally avoided desert climates during both the Maastrichtian and the recovered Danian ecosystems (fossil plots in Fig. 6g, h). However, during the first few years after the impact, mammals likely occupied extensive cold-desert and tundra regions outside the highest latitudes. In newly formed cold deserts, where pre-impact vegetation had largely died, mammals associated with detritus-based food webs could survive by feeding on dead plant material, seeds, nuts, and roots. In relatively warm tundra regions, small mammals with underground nests may have utilized roots, seeds, and seasonally available mosses during short growing seasons.

Accordingly, mammalian habitat distributions were reconstructed primarily from climate classifications and surface air temperatures. High-diversity habitable regions occurred in tropical, temperate, newly developed desert, and steppe climates, whereas lower-diversity habitats extended into cooler steppe, cold, and parts of tundra regions (Figs. 5e–h, 6g, h). Despite severe climatic disruption, the total habitable area for mammals likely declined by only ~10% during the coldest interval after the impact relative to pre-impact conditions, substantially less than for non-avian dinosaurs and birds (Fig. 5g, Table 1).

Survival migration to new refuges

Survival migration likely began within days after the impact, triggered by extensive wildfires caused by intense infrared radiation from ejecta re-entry. These fires drastically reduced vegetation cover and population sizes, forcing surviving animals to move away from heavily burned regions. Although terrestrial biomass declined sharply, deserts and sparsely vegetated areas may have served as temporary refugia where animals could survive on residual vegetation, roots, insects, and detritus. Birds particularly benefited from flight capability, allowing rapid movement to unburned areas and access to scattered food resources.

By approximately five months after the impact, climate simulations indicate the development of mildly wet conditions at low latitudes, around 15°–25°N in the Northern Hemisphere and 20°–30°S in the Southern Hemisphere. These regions corresponded to former subtropical deserts that transitioned into temperate, rain-bearing climates with recovering vegetation (Fig. 7b, c, e, f). Strong solar insolation at low latitudes further promoted plant regrowth and increased the survivability of these refugia (Fig. 7a, d). Consequently, surviving animals likely migrated progressively from mid-latitude regions toward newly formed low-latitude temperate refuges.

A plausible migration pathway includes movement from western Europe (40°–50°N) to southwestern Europe (30°–40°N) within the first several months after the impact, followed by southward migration into southwestern Africa (15°–25°N), where populations may have persisted for several years before recolonizing higher latitudes as climates recovered. Similar migration routes are inferred from eastern Europe into southwestern Asia and from southern South America into central western South America (Fig. 7e, f).

Birds and crocodilians inhabiting mid-latitude regions would therefore have required migration toward lower-latitude refugia to survive (Fig. 6a, c). Birds relied primarily on flight, whereas crocodilians likely dispersed through swimming and short overland movements. Mammals were less capable of long-distance migration but benefited from broader refuge availability, including underground shelters and access to roots and invertebrates. These ecological advantages likely contributed to their relatively high survival rates during both the infrared radiation phase and the subsequent impact winter (Fig. 6d).

Limitations of this study and directions for future work

Uncertainties remain regarding the relative climatic roles of soot, sulfate aerosols, dust, and wildfire-derived emissions following the Chicxulub impact[12, 13, 40]. However, both soot- and sulfate-dominated scenarios produce similar post-impact climates characterized by narrow temperate refugia surrounded by predominantly cold and dry environments. Consequently, these uncertainties do not substantially affect the main conclusions regarding differential survival among vertebrate groups.

The primary focus of this study is to use climate-model reconstructions of terrestrial tetrapod distributions to infer survival strategies during the immediate aftermath of the impact, a period that is not directly documented by the fossil record. These reconstructed distributions are then compared with fossil distributions before and after the impact to provide a comprehensive assessment of changes in faunal composition and biogeographic patterns across the K–Pg boundary. Although sampling bias is inherent in paleontological data, it is unlikely to alter the relative diversity patterns observed or the conclusions of this study. Moreover, Maastrichtian and Danian intervals are of comparable duration, and both species- and genus-level datasets exhibit consistent trends.

The reconstructed climate and vegetation patterns identify potential refugia that are broadly consistent with fossil distributions, suggesting that subtropical deserts temporarily served as temperate refugia for birds, whereas non-avian dinosaurs lacked sufficient habitable area to maintain viable populations. Future work should focus on discovering additional Danian fossils, particularly birds from arid regions and crocodilians from tropical K–Pg boundary sections. Expanded Danian fossil records will improve occurrence datasets and provide stronger constraints on post-extinction survival and dispersal pathways.

Mechanisms for extinction and survival

The Chicxulub impact triggered a cascade of environmental disturbances, including intense infrared radiation from reentering ejecta, global wildfires, and prolonged climatic cooling driven by stratospheric aerosols. Our climate–ecological simulations suggest that these processes acted sequentially to determine the extinction and survival patterns of terrestrial tetrapods across the K–Pg boundary.

Infrared radiation generated by reentering ejecta likely caused severe mortality among exposed terrestrial vertebrates immediately after the impact. Thermal radiation reaching Earth's surface may have been equivalent to repeated megaton-scale explosions on a global scale, resulting in widespread mortality among animals inhabiting surface environments. Most non-avian dinosaurs and pterosaurs were therefore likely eliminated during this initial phase. However, thermal radiation alone cannot explain the observed selectivity of survival among tetrapod groups.

The prolonged impact winter that followed appears to have been the principal driver of the mass extinction. Stratospheric soot and sulfuric acid aerosols reduced incoming solar radiation, causing severe global cooling and a sharp decline in net primary productivity (NPP). The resulting collapse of terrestrial ecosystems drastically reduced habitable area and food availability. Large-bodied non-avian dinosaurs, which required abundant plant biomass and prey resources, were unable to persist under these conditions. Even if small populations survived the initial thermal effects, subsequent habitat loss and ecosystem collapse would have prevented their long-term survival.

In contrast, birds, crocodilians, and mammals possessed ecological traits that enhanced survival. A small proportion of birds may have survived the initial catastrophe by sheltering underground or in aquatic environments. Their flight capability subsequently enabled migration to transient climatic refugia that developed in low-latitude temperate zones, including temporarily vegetated subtropical desert margins and tropical oceanic regions. These refugia supported sparse vegetation and invertebrate communities, providing minimal food resources during the impact winter. Small body size, relatively low energetic demands, and flexible diets further increased avian survival potential. As climate and vegetation gradually recovered over approximately 15 years, surviving bird populations likely recolonized their former habitats.

Crocodilians survived primarily through the buffering effects of aquatic habitats, which reduced exposure to thermal radiation and short-term environmental fluctuations. However, prolonged cooling substantially restricted suitable habitat, confining surviving populations to low-latitude warm regions in parts of Africa and the Americas. Their ability to disperse through freshwater and coastal environments likely facilitated persistence and subsequent range expansion during climate recovery.

Mammals exhibited the highest survival potential among terrestrial tetrapods. Underground sheltering protected them from both thermal radiation and climatic cooling, while access to roots, seeds, insects, and detritus enabled survival under conditions of greatly reduced primary productivity. Consequently, mammals retained relatively broad habitable areas throughout the recovery interval and were able to expand ecologically after ecosystem recovery.

The modeled changes in habitable area are broadly consistent with fossil occurrence patterns across the K–Pg boundary and provide a framework for linking short-term environmental disruption with long-term ecological and evolutionary outcomes. Following ecosystem recovery and the disappearance of dominant large-bodied terrestrial vertebrates, mammals expanded into newly available ecological niches and diversified rapidly. Overall, our results indicate that survival during the K–Pg crisis depended primarily on refuge availability, dispersal capacity, and tolerance to prolonged reductions in temperature and primary productivity. These factors ultimately determined the contrasting extinction and survival patterns observed among terrestrial tetrapods.

Methods

Although impact-driven extinction would have unfolded within the first 1–3 years after the event, the temporal resolution of fossil occurrence data is too coarse to resolve such short-term processes directly, because extinction rates and biodiversity are generally compiled as aggregated values for broader geological intervals. Accordingly, this analysis tests whether extinction and survival were driven by infrared radiation and global cooling by comparing survival rates and species richness with changes in habitable area inferred from climate-driven environmental change. In this sense, the present study uses model-based reconstructions of climate and habitable zones to capture short-term shifts in animal distributions that are effectively invisible in the fossil record. Comparison of the fossil data with habitable regions estimated from the climate model in this study further supports this interpretation (Fig. 6).

First, we compiled the distributions of surviving lineages and the numbers of species and genera for four representative terrestrial animal groups across the Maastrichtian and Danian, spanning the mass extinction event, and evaluated their survival rates and ecological characteristics. Second, we reconstructed global paleoclimate classification maps for the pre- and post-impact intervals. Third, we generated global maps of net primary productivity (NPP) for both timeframes, incorporating the effects of abrupt global infrared radiation immediately after the impact and the subsequent climate cooling.

Fourth, we estimated habitable areas for birds and non-avian dinosaurs based on NPP. Fifth, we reconstructed habitable areas and diversity patterns for crocodilians and mammals using monthly temperature data and climate classification maps, respectively. Sixth, we compared fossil distribution maps with minimum survival-area estimates to reconstruct post-impact survival migrations.

As a result, we were able to explain why the post-extinction and post-recovery fossil distributions resemble pre-extinction distributions despite the occurrence of a major transient crisis. In this study, the climate–ecology analysis specifically targets the abrupt environmental perturbation, whereas the fossil record mainly reflects the slower and more stable phases before and after the crisis. By combining these two approaches, we can reconstruct a sequence of stable conditions → abrupt environmental disruption → subsequent stabilization or gradual evolutionary recovery.

In conclusion, this framework clarifies the mechanisms underlying selective extinction and survival responses to infrared radiation and short-term climate cooling following the end-Cretaceous asteroid impact.

Fossil data acquisition and preparation

Occurrence data for Dinosauria, Aves, Avialae, Crocodylomorpha, and Mammalia were retrieved from the Paleobiology Database (PBDB; https://paleobiodb.org) via the PBDB Navigator on October 11, 2025. Fossil occurrence data were filtered by taxonomic group and geological age, with primary emphasis on the Maastrichtian (6.2 Myr) and Danian (5.3 Myr), to generate fossil-occurrence distribution maps. For the diversity panels in Fig. 1, taxonomic data from the Paleocene (10.0 Myr) and Paleogene (43 Myr) were additionally compiled. For non-avian dinosaurs, only Maastrichtian data were used. To isolate non-avian dinosaur occurrences, all records assigned to Aves and Avialae within the Dinosauria dataset were removed. The data were processed using Microsoft Excel (Version 2511; Microsoft Corp.), employing functions such as IF and COUNTIF for taxonomic counting and data organization.

Taxonomic standardization and occurrence counting

Raw occurrence data were used for both plotting and total occurrence counts. In determining genus richness, occurrences of ichnotaxa and ootaxa were excluded to avoid overlap with skeletal remains. Within Crocodylomorpha, *Holops* was excluded as it is currently considered an invalid subtaxon of *Thoracosaurus* in the PBDB. For Maastrichtian avian records, all neornithine occurrences were excluded with the exceptions of *Vegavis* and *Asteriornis*. Other Maastrichtian fossils previously attributed to Neornithes were omitted due to insufficient identification from fragmentary specimens[41–43] and subsequent studies questioning their validity[44–48].

Genus list was generated by filtering occurrences with an "accepted rank" of "genus" and identifying unique "accepted name" entries. To ensure completeness, genera present in "accepted rank" of "species" but missing from the "accepted rank" of "genus" were integrated into the final genus-level counts. Genera were then quantified by removing duplicate generic names from the combined dataset. The resulting genus counts were visualized using bar charts, and all occurrence data were projected onto paleogeographic reconstructions.

Identification of surviving taxa

Surviving genera defined as those present in both the Maastrichtian and Danian assemblages. Occurrences of these surviving taxa were extracted for plotting and counting. The list of surviving genera was generated using the same methodology described above. Occurrences of these surviving genera were also projected onto the paleogeographic reconstructions alongside all occurrence data.

Analysis of surviving lineages

To track survivorship beyond the K–Pg boundary, lineages common to both the Maastrichtian and Danian were identified, excluding non-avian dinosaurs. Because taxonomic ranks were not consistent among groups, we selected representative lineages that were well represented in the fossil record and could be clearly identified within the Paleobiology Database (PBDB) taxonomic hierarchy. Specifically, we selected lineages that were recognized as distinct taxonomic units in the PBDB and contained sufficient occurrence records in both the Maastrichtian and Danian intervals to allow meaningful comparison across the K–Pg boundary. For birds, these included non-neornithine Ornithurae and Neornithes; for crocodilians, Crocodylia, *Borealosuchus*, Sebecosuchia, and Dyrosauridae; and for mammals, Eutheria, Metatheria, and Allotheria. Although Pholidosauridae was identified as a surviving lineage based on the occurrence data of Crocodylomorpha, it was excluded from genus-level counts because no specific genera were definitively identified within those records. Taxonomic affiliations were determined by tracing the "parent taxon" hierarchy within the PBDB. Occurrence, species, and genus counts for these lineages followed the same exclusion criteria and methodology described above. Genus counts for these lineages were visualized using pie charts to illustrate shifts in taxonomic composition.

Paleogeographic reconstruction of occurrence data

Paleolatitudes and paleolongitudes of occurrence data at the K–Pg boundary (66 Ma) were reconstructed using GPlates (v2.5.0)[49] and QGIS (v3.30.1)[50]. Tectonic reconstructions were based on the PALEOMAP Global Plate Model[51]. The occurrence dataset, including geographic coordinates and GPlates-compatible Plate IDs, was formatted in CSV (UTF-8). For records with missing or incomplete Plate IDs, appropriate IDs were manually assigned within the GPlates interface. The validated dataset was then imported into QGIS and exported as an ESRI Shapefile to ensure compatibility with GPlates. These Shapefiles were subsequently loaded into the GPlates project as occurrence layers.

In GPlates, we integrated the PALEOMAP PaleoAtlas (v3) rotation model (PALEOMAP_PlateModel.rot) and plate polygons (PALEOMAP_PlatePolygons.gpml). The reconstruction was set to 66 Ma to generate paleogeographic coordinates. Finally, the reconstructed occurrence layer was overlaid onto a custom paleomap, which was developed using the 66 Ma PaleoAtlas base map and paleo-coastline data from Burgener et al.[31].

While taxonomic analyses were conducted at the occurrence, species, and genus levels, only genus-level results were used for visualization in all figures (bar charts, pie charts, and paleomaps). Accordingly, separate layers of ‘all occurrences’ and ‘occurrences of surviving genera’ were exported at the genus level for final plotting.

Climate model calculations

Recent findings suggest that **soot from impact sites**, rather than dust or wildfires alone, was the primary driver of "impact winter" and mass extinction[13]. The severity of extinction varied with the impact site's geology—organic-rich areas produced more soot, amplifying cooling. In contrast, location-independent mechanisms (e.g., dust, infrared radiation, wildfire) fail to explain observed extinction frequencies.

In this study, we investigated the global and regional climate changes triggered by the Chicxulub impact using climate modeling by input of soot and sulfuric acid aerosols formed from impact target rocks into the stratosphere. Building on our previous research, we employed climate model simulations for two distinct scenarios: one focused on stratospheric soot aerosols (soot scenario)[11, 13, 32] and another on stratospheric sulfuric acid aerosols (SO_2 scenario). The amount of soot released was estimated based on the organic carbon content of the target rocks at Chicxulub[11, 13], while the SO_2 release was calculated from the sulfur content of the rocks melted by the impact (see Methods).

We utilized the results from the Meteorological Research Institute's coupled atmosphere-ocean global climate model, MRI-CGCM3[52], detailed in Kaiho et al.[11], for the impact soot scenarios. The model consists of an atmospheric general circulation model with a land surface model, an ocean circulation model accounting for sea ice, and an aerosol chemical transport model. The atmospheric model has a horizontal resolution of about 120 km (TL159) with 48 vertical layers, extending from the surface to a model top of 0.01 hPa (~80 km altitude). For further details on model evaluations, refer to Kaiho et al.[11]

Kaiho et al.[11] conducted climate model calculations with varying amounts of soot (black carbon, BC) ejected by the asteroid impact on the northern Yucatan Peninsula, based on modern preindustrial climate settings. The BC was injected into one column of the model grid at 21°N, 90°W (Yucatan Peninsula), over a one-day period on June 1st in the first year after the impact. The BC was vertically distributed as 62%, 20%, and 18% over the altitude ranges of 0–10 km, 10–30 km, and 30–50 km, respectively, with equal spreading at each level, derived from Saito et al.[53]. We used the results of 15-year model experiments for the soot-impact cases (1500-Tg BC and 2600-Tg BC cases) and a 30-year no-impact control experiment with no BC ejection (the “pre-impact case” for the soot scenario)[11].

Additionally, we conducted a 15-year model experiment using the Meteorological Research Institute Earth System Model version 2.0 (MRI-ESM2.0)[54, 55] for the impact SO_2 scenario (stratospheric 2000-Tg SO_2 case), along with a 30-year no-impact control experiment with no SO_2 ejection (the “pre-impact case” for the SO_2 scenario). MRI-ESM2.0 consists of an atmospheric general circulation model with land processes (MRI-AGCM3.5), an ocean-sea-ice circulation model, an aerosol chemical transport model, and an atmospheric chemistry model. The horizontal

resolutions for the atmospheric, aerosol, and chemistry models are 120 km (TL159), 180 km (TL95), and 280 km (T42), respectively, with 80 vertical layers reaching up to 0.01 hPa. The aerosol model treats the physical and chemical processes including emission, transport, diffusion, chemical reactions, sedimentation, and dry and wet deposition of aerosols (sulfate, black carbon (BC), organic carbon (OC), dust, and sea salt) and their precursor gases. Because the model does not treat nucleation and coagulation of aerosols, it assumes prescribed lognormal size distributions for sulfate, BC and OC, and the size distribution of stratospheric sulfuric acid aerosols is based on present-day observations[54, 56], although the size distributions of dust and sea salt are represented by 10 discrete size bins. Although the particle size distribution of dry sulfate aerosols is prescribed, it can vary depending on the relative humidity mostly in the troposphere. The SO_2 was injected into the stratosphere (20–50 km in altitude) within the single grid cell with approximate horizontal resolution of 180 km containing the impact site, over a one-day period on June 1st in the first year, same as the soot scenario. The SO_2 injection was modeled to represent 100 times the amount of SO_2 emitted during the 1991 Mt. Pinatubo eruption (2000 Tg in the stratosphere), assuming preindustrial climate conditions. Note that the climate models have limitations to simulate the destructive effects of the asteroid itself and the short-term local extreme atmospheric changes that occurred immediately after the impact. However, the models can estimate the climate changes caused by aerosols after the three-dimensional spread of the aerosols by atmospheric transport after the asteroid impact.

To summarize the model calculations used in this study, we used the results from the MRI-CGCM3 calculations for 15-year 1500-Tg BC case (stratospheric 350-Tg BC, impact case), the 15-year 2600-Tg BC case (stratospheric 600-Tg BC, stronger-cooling impact case), and the 30-year control experiments with no BC injection (the "pre-impact case" for soot) and those from the MRI-ESM2.0 calculations for the 15-year stratospheric 2000-Tg SO_2 case and the 30-year control experiment with no SO_2 injection (the "pre-impact case" for SO_2)[11]. Note that we conducted separate no-impact control experiments for the soot and SO_2 cases using MRI-CGCM3 and MRI-ESM2.0, respectively. Following Kaiho et al.[11], we assessed the climate response, including surface air temperature, SST, precipitation, winds, atmospheric circulation, radiation, and soil moisture, by subtracting the monthly climatology (30-year mean) of the corresponding control experiment from the monthly mean results of the impact scenarios.

In this analysis, soil moisture saturation calculated by MRI-CGCM3 and MRI-ESM2.0 was used as a threshold for vegetation loss and the potential for regrowth. The land surface model employs 13 vegetation types and 14 soil layers, with a total depth of 10 m and finer intervals near the surface (6 layers within the top 50 cm). The degree of soil moisture saturation averaged for depths 0–5 cm was applied for Figure 7c, f, Supplementary Figures 5u–x and 6u–x. Note that the model does not treat the dynamic vegetation; the vegetation types are fixed throughout the calculation. During periods of a significant decrease in surface air temperature, especially in tropical regions, soil moisture levels might be overestimated as the model maintains forest conditions even after forest devastation[57, 58].

Amounts of soot from impact target rocks: The amount of stratospheric soot formed from target rocks is calculated using the equation:

$Vc \times 2.3 \times 1000 \times 0.003 \times EF \times SFs \times SFl$

where:

- *Vc* is the combustion volume of sedimentary rocks,
- is the density of sedimentary rock in g/cm³,
- is the total organic carbon (TOC) content,
- *EF* is the soot emission factor, ranging from 0.03 to 0.1,
- *SFs* represents the survival fraction of soot from combusted dust from sedimentary rocks in the stratosphere for global distribution in the first month (short term), the minimum value is 0.53 from Figure 2 of de Niem et al.[59] by a factor of 2 at 80 seconds for 30 second after the impact derived from the right panel of Figure 4 in Saito et al.[53]. The height of the base of the stratosphere is set at 17 km.
- *SFl* represents the survival fraction of soot in half year (long term): amount of soot in the second to sixth month/that in the first month, 600/1,100 = 0.55.[11, 32]

For the Chicxulub impact, with a combustion radius of 35 km and a sedimentary rock thickness of *3* km, *Vc* ($1/3 \times 3.14 \times 3 \times [3 \times 35^2 - 3^2]$) equals 11,500 km^3. The amount of soot formed from target rocks is estimated to be 690–2,300 Tg BC. This study selected a stronger cooling impact case, corresponding to 600 Tg BC for the stratosphere the second to sixth months after the impact[11, 13, 32] (Fig. 2b–d, Supplementary Fig.3i–o).

Amounts of SO_2 from impact target rocks: The amount of SO_2 in the stratosphere formed from the Chicxulub target rocks is calculated using the equation:

$Vm \times 2 \times 1000 \times 0.013 \times 0.4 \times 0.03 \times 2$,

where:

- *Vm* is the melting volume of sedimentary rocks,
- the first "2" represents the sedimentary rock density (g/cm^3),
- is the total sulfur (TS) content for the target sedimentary rock at Chicxulub,
- is the sulfur emission factor[32],
- represents the survival rate, defined as the average ratio of SO_4 amounts in the HR curve (which does not account for the coagulation effect of sulfuric acids) to the LTS curve (which includes the coagulation effect), both required to induce a 12 °C global surface cooling (as shown in Fig. 2 of Kaiho and Oshima[13]).
- The second "2" is the mass ratio to sulfur (S).

For the Chicxulub impact, with a melted radius of 15 km and a sedimentary rock thickness of *3* km, *Vm* (1/3 × 3.14 × *3* × [3 × 15^2 – *3*^{2}]) equals 2,100 km^3. The amount of SO_2 formed from target rocks is estimated to be 44,000 × *SR* Tg SO_2. The amount of stratospheric SO_2 formed from target rocks ranges from 1,300 to 35,000 × *SR* Tg SO_2, based on stratospheric SO_2 retention rates of 3%[32, 33] and 80%[60], respectively, for total SO_2 and SO_3. The amount of stratospheric soot formed from target rocks ranges from 170 to 4,500 Tg SO_2, with an average of 2,400 Tg SO_2, based on a 13% fraction entering the stratosphere from ejecta density distribution after the Chicxulub impact (Figure 2 of de Niem et al.[59]). This study used an estimate of 2,000 Tg for stratospheric SO_2 (Supplementary Fig. 3q–w).

Total amount of soot deposited on Earth

Soot has been proposed to derive mainly from two sources: global wildfires and the impact site itself[11, 40]. The ratio of polycyclic aromatic hydrocarbons (PAHs), expressed as the coronene index, at the K–Pg boundary indicates a high-energy combustion source far exceeding background forest fires[61]. In addition, the similarity of PAH molecular ratios between proximal and distal sites and the distribution of PAHs suggests that much of the soot was generated from the target rocks of the Chicxulub impact[11, 62]. Molecular and charcoal evidence further indicates that wildfires occurred later and were more prolonged[63]. Climate simulations by Bardeen et al.[40] assumed atmospheric injection of 15,000 Tg soot, following Wolbach et al. and a fine-soot fraction[40, 63]. Assuming that half of the soot fell on wetlands and the other half into the oceans, with 90% of the oceanic fraction deposited on continental shelves and 10% in the deep ocean, the concentration factor of fallout particles on shelves is estimated as 2.1 = (1 + 1 × 0.5 × 0.90) / 0.7, where 1 denotes direct atmospheric deposition, the second term denotes land-derived input, and 0.7 is the estimated depositional-area fraction of continental shelves[64]. Using this enrichment factor, the original estimate of 15,000 Tg was revised to 7,000 Tg BC.

Most soot generated by large wildfires remains in the troposphere; for example, only 2–2.5% of soot from recent major wildfires in Canada in 2017 and Australia in 2019–2020 reached the stratosphere[65, 66]. By contrast, global infrared radiation generated by impact ejecta re-entry may have ignited forests almost instantaneously and lofted soot to higher altitudes[40]. At the same time, large amounts of water vapour released by the ocean impact may have promoted rainfall in many regions and locally suppressed fire spread. Given this uncertainty in fire distribution, the habitat reconstructions shown here were drawn conservatively, allowing for the possibility that some dinosaurs sheltered in forests survived the infrared-radiation phase.

The revised estimate of 7,000 Tg BC includes (1) infrared-radiation-induced forest fires, (2) combustion of impact target rocks by impact energy, (3) burning of dead vegetation under low-latitude aridification during the four years after the Chicxulub impact, and (4) later background wildfire activity. This interpretation is supported by evidence that some wildfires occurred between the impact and tsunami arrival[67], whereas molecular and charcoal data indicate delayed and prolonged burning[62]. Thus, only part of the 7,000 Tg BC was likely injected into the atmosphere by infrared-radiation-induced forest fires. Assuming that the fraction of soot reaching the stratosphere was low for wildfires but high for impact-derived soot based on Ref. 11, 61 and 62, model calculations were performed using soot released from the impact site[11]. Of this amount, 1,100 Tg BC represents soot present in the atmosphere during the first month after the impact, whereas 600 Tg BC represents the atmospheric burden during months 2–6, as shown in Fig. 2 of Kaiho et al.[11]. In the present study, the 600 Tg BC value was shown as the soot loading responsible for global cooling. Because stratospheric soot can only be estimated indirectly from total organic carbon in sedimentary rocks, burned volume and injection efficiency, the relative contributions of infrared-radiation burning, dry-climate burning and later wildfires remain uncertain.

Total amount of sulfur deposited on Earth

Because most sulfur released by the impact entered the atmosphere as SO_3[33], it was rapidly converted to sulfuric acid and therefore became more likely to fall out together with dust and other particles. Sulfuric acid that was removed before spreading far from the impact site would not have contributed to global sunlight reduction or cooling. Therefore, the globally dispersed sulfur inventory was estimated from sulfur

abundances in impact layers sufficiently distant from the impact site. Accordingly, sulfur data from North America were not used; instead, sulfur abundances from Europe were used to calculate the amount of sulfur that was globally dispersed (Supplementary Table 11).

Our estimated SO_2 emission (2000 Tg [2 Gt] SO_2) is based on the sulfur content of impact target rocks and their injection into the global stratosphere[13]. An independent estimate of ~1700 Tg [1.7 Gt] SO_2 is derived from sulfur concentrations measured in European marine K–Pg boundary sections[14] (Supplementary Table 11).

We assume that 50–60% of atmospheric sulfur deposited on land is retained in vegetation and soils, whereas the remaining 40–50% (0.45 in average) is transported to the ocean[68]. Of the sulfur delivered to the ocean, 90% (0.90) is assumed to accumulate on continental shelves and slopes, with the remaining 10% reaching the deep ocean, based on modern observations[69].

Under these assumptions, sulfur deposition on continental shelves and slopes is enriched by a factor of ~2 relative to direct atmospheric input. This enrichment factor is calculated as:

$$2.0 = (1 + [1 \times 0.45 \times 0.90]) / 0.7,$$

where 1 represents direct atmospheric deposition, the second term represents land-derived sulfur input, and 0.7 is the estimated depositional area fraction of continental shelves[64].

Validity of climate model calculations

Our model calculations in Kaiho et al.[11] uses the higher horizontal resolution among climate models to reconstruct K–Pg climate change, exceeding four times the resolution of other modern Earth models and over 20 times the resolution of other end-Cretaceous models shown in Figure 5 in Kaiho and Oshima[32]. The high horizontal resolution enables the identification of climate zones in small areas, such as temperate regions that emerged within subtropical deserts on plains and in oceanic tropical regions. Such features are generally difficult to resolve using previous Cretaceous climate models. Building on previous work, we used impact-induced stratospheric soot aerosol model calculations from Kaiho et al.[11] and extended our research by including new climate model calculations on stratospheric sulfuric aerosols.

Both the impact case (1500-Tg BC) and the stronger-cooling impact case (2600-Tg BC, soot case) resulted in temperature reductions of 6°C and 8°C, respectively, around the Gulf of Mexico over the ten years following the impact (Figure 7b in Kaiho et al.[11]). These findings align with the observed 7°C cooling in the same region, as indicated by geochemical records[70]. Additionally, both cases showed global surface cooling of 10°C and 12°C, corresponding to land temperature decreases of 16°C and 18°C[32]. This level of cooling could account for the survival of crocodilians, which depended on detritus-based food chains and temperature more than 19°C[71] (Table 1, Supplementary Tables 12, 13). We selected the stronger-cooling case as the primary model scenario because it resulted in a more significant reduction in habitable areas for the tetrapod groups, making it a more plausible explanation for their extinction and survival (Supplementary Fig. 3, Supplementary Table 10).

Previous models assumed that the impact generated large amounts of stratospheric sulfuric acid aerosols[60, 72]. However, impact experiments indicate that at least ~3% of the ejected sulfur persisted as aerosols after the impact[32, 33], a result supported by additional experimental studies[73, 74]. Given the large uncertainty in sulfur survival in the atmosphere (approximately 3–100%, representing ~30-fold variability), the model calculations by Kaiho et al.[11] and Kaiho and Oshima[32] instead focused on soot derived from target rocks as the primary driver of extinction, based on the abundance of five- to six-ring polycyclic aromatic hydrocarbons (PAHs) and organic carbon observed at both proximal and distal sites.

In this study, we present results for both soot and SO_2 emission scenarios (Fig. 2 and Supplementary Figs. 8 and 9). Both scenarios produce broadly similar climate responses; however, the soot emission scenario shows a greater reduction in surface shortwave radiation and longer cooling, whereas the SO_2 emission scenario exhibits faster recovery (Supplementary Figs. 8 and 9). Climate classification changes during the first year, the coldest year, and the mid-recovery phase are also similar between the two scenarios, although climate change is greater in the soot scenario (Fig. 2). To clearly demonstrate the climate responses, we use the soot emission scenario to estimate terrestrial net primary productivity (NPP) and habitable areas for birds, non-avian dinosaurs, crocodilians, and mammals.

The model calculations did not consider the simultaneous injection of soot, SO_2 and water vapor. The strong light absorption due to the large amount of stratospheric soot may suppress photolytic reactions and thereby reducing the conversion of SO_2 into sulfuric acid aerosols. On the other hand, the injection of water vapor may lead to increase sulfuric acid aerosols, which may coagulate with stratospheric BC particles, increasing their particle size and resulting in a shorter atmospheric lifetime. Because of these complex interactions, shown as examples, there are limitations and uncertainties in quantifying these effects in models. However, even in the soot-only scenario, the decrease in solar radiation is significant enough (more than 85% and sufficiently dark [Supplementary Figs. 8 and 9])[11], and therefore the presence of additional sulfuric acid aerosols may contribute more to prolonging the cooling period than to reducing solar radiation. Even if the cooling period were prolonged

by 1–2 years, the animals that became extinct would still have perished due to soot-induced cooling; therefore, neither Figure 6 nor the conclusions would change. Therefore, this study demonstrates that extinction and survival patterns can be explained under the assumption of either soot or sulfuric acid aerosols.

Low-latitude surface temperature during the Maastrichtian (transitional climate, average surface temperature 14 °C) was 5 °C higher than that of the modern Earth (coldhouse climate, average surface temperature 9 °C)[75]. There are no significant differences (approximately 0 °C) in modeled surface air temperatures on land between 20°–30° latitude in both hemispheres, or in modeled sea surface temperatures (SSTs) between 20°N and 30°S[76]. In our analysis, we used the Maastrichtian climate by methods of transfer from the Maastrichtian climate classification global map to the climate classification global map after the impact and correction from modern Earth surface temperature to Maastrichtian surface temperature. only temperature anomalies or rate-of-change values to explain species survival in low-latitude regions (Supplementary Figs. 8 and 9). To assess survival or extinction potential, surface temperatures on modern land were translated to end-Cretaceous conditions using data from Ref. 76 (Supplementary Tables 10, 12).

Among existing studies, only Upchurch et al.[76] provides estimates of land surface temperatures across all latitudes at the end of the Cretaceous. In this study, we used surface temperature data from Judd et al.[75] and land surface temperature data from Upchurch et al.[76]. Note that land surface temperature differs from general surface temperature due to the influence of large subtropical deserts located between 20° and 30° latitude in the modern Earth. If land surface air temperatures between 20°–30° latitude during the end-Cretaceous were 5 °C higher than those of today, our results on crocodilian extinction in those latitudes remain consistent (see Supplementary Tables 10, 12).

Köppen climate classification maps

First, we created Köppen climate classification maps for the modern Earth using grid point data of the monthly mean surface air temperature and precipitation obtained from climate model calculation results for the pre-impact, impact soot, and impact SO_2 cases in the first, second, third, fourth, fifth or sixth, seventh, and 15th year after the impact (Supplementary Fig. 3), with the help of Excel VBA and ArcGIS. Next, from the modern map, we read climate zone change patterns for the first year after the impact, the coldest year, and the mid-recovery year on surface temperature and 0–500 m elevation in modern Earth to make Supplementary Table 3. Finally, we applied the climate zone change patterns for the three periods to the Maastrichtian climate classification map of Burgener et al.[31] to produce Köppen climate classification maps for the end-Cretaceous to the earliest Paleogene Earth (Fig. 2). Supplementary, detailed distributions of climate classifications were reformed for the mid-recovery year based on the modern Köppen climate classification maps because of the complicate distribution.

Terrestrial net primary productivity

This section explains the procedure for creating figures that illustrate the global distribution of vegetation (Fig. 3a–e). Plants require an appropriate level of sunlight depending on their species. To reconstruct vegetation before and after the asteroid impact at the end of the Cretaceous, we first calculated terrestrial net primary productivity (NPP) for low latitude regions in the low latitudes of the modern Earth after the impact using the Miami model[34]. In this calculation, the NPP value was obtained by multiplying the Miami model NPP by the sunlight ratio (SR), which depends on sunlight reduction by soot, and wildfire reduction factor (WFR; 0.5 for the first year after the impact, except for pre-impact desert regions; 1.0 for all other cases; Supplementary Tables 7).

NPP was calculated using both a temperature-based and a precipitation-based equation, with the lower value adopted as NPP. Total NPP was estimated by multiplying the net primary productivity (NPP) of each climate classification based on stratospheric soot (Fig. 3b–d; Supplementary Table 14), a sunlight impact ratio, and 0.5 for the first year considering effect of the global infrared radiation (SIR, Fig. 3). To know which equation results are lower, we also calculate NPP in low and middle latitudes. The results are NPP based on precipitation is lower in 55°N–55°S latitudes and NPP based on temperature is lower in the higher latitudes (Supplementary Table 15).

The calculated NPP values for each climate classification and vegetation type (Supplementary Tables 14, 16) were applied to the Köppen climate classification map (Fig. 2) to reconstruct NPP distribution maps. Based on the NPP data from representative low-latitude regions, we determined the NPP values at the boundaries of low-latitude climate zones after the impact (0.11, 0.20, 0.30 kg C m^{-2} yr^{-1} in NPP).

Terrestrial net primary productivity (NPP) was calculated from annual averaged temperature (T [°C]), annual precipitation (P [mm]), and the plant biomass ratio (R) in response to decreasing downward shortwave radiation:

NPP (kg C m^{-2} y^{-1}) = min {3/(1 + exp [1.315 – 0.119T])*R, (3 (1- exp [– 0.000664P]))*R}

min: selected a minor value from two values based on T or P.

The sunlight impact ratio (SIR) is given by the equation: R = SW*0.67 + 0.27 (SW: downward shortwave radiation ratio). This equation was the correlation formula derived from experimental data presented in Supplementary Table 17. The NPP and process of calculations in low latitudes

in each region are shown in Supplementary Table 7.

Total NPP, including contributions from mid- and high-latitude regions, was estimated by multiplying the net primary productivity (NPP) of each climate classification and vegetation type (Supplementary Table 5) by a sunlight impact index, and by applying a germination temperature threshold of 6 °C in monthly mean temperature for Arctic plants[77]. This threshold corresponds to the mid-temperature of tundra climates, set at the boundary value of 0.11 NPP (the boundary between pale yellowish green and gray in Fig. 3b, c), which also corresponds to the boundary of hot desert and semidesert climates. Boundary lines were drawn based on temperature distributions in July and January reported by Upchurch[76]. With the exception of refuge areas, NPP values were reduced by half during the first year after the impact due to global wildfires (Supplementary Table 7). Figure 3a–e were produced using these data.

Ecological model for each tetrapod animal group

This section describes the methodology used to construct figures illustrating the global distributions of birds, non-avian dinosaurs, mammals, and crocodilians during the first month, the first to third years, and the sixth year following the Chicxulub impact (Figs. 4 and 5). The maps for the first month represent the effects of intense global infrared radiation produced by reentering ejecta immediately after the impact, followed by abrupt sunlight reduction and global cooling caused by stratospheric soot aerosols. The first year corresponds to the interval of minimum solar irradiance at Earth's surface, the third year represents the coldest climatic conditions, and the sixth year marks a phase of partial environmental recovery.

During the first month after the impact, non-avian dinosaurs and birds were severely affected by global infrared radiation because they lacked effective shelter from this radiation, resulting in very low survival rates (Supplementary Table 6). In contrast, the abundances of sheltered animals—mammals and crocodilians—were reduced by one rank, reflecting partial protection from infrared radiation as well as impacts from widespread wildfires, abrupt sunlight reduction, and subsequent global cooling.

For the pre-impact period, the first to sixth years after the impact, and the recovery phase, the global distributions of four animal groups are shown on paleogeographic maps based on the abundance criteria defined for each group in Supplementary Table 8 (Figs. 4 and 5). The distributions of birds and non-avian dinosaurs (Fig. 4) were generated using net primary productivity (NPP) maps (Fig. 3; Supplementary Table 8). The distributions of crocodilians (Fig. 5a–d) were derived from habitable surface air temperature data, whereas those of mammals (Fig. 5e–h) were based on climate classification maps (Fig. 2; Supplementary Table 8).

For non-avian dinosaurs, distributions explicitly exclude newly emergent temperate regions within pre-impact subtropical desert climate zones, based on the climate classifications presented in Table 1 and Supplementary Table 8. In addition, areas severely affected by burning in the vicinity of the Chicxulub impact site were excluded from post-impact distributions.

Declarations

Acknowledgments

We thank Seiji Yukimoto and Makoto Deushi of Meteorological Research Institute for providing helpful comments on the meteorological analysis; Tomoyuki Ohashi, and Tai Kubo for paleontological discussion; Tomoyuki Shibuki and Arihito Kondo for producing modern climate maps, and Melanie During and anonymous referees for useful comments.

Funding

This study was supported by the Japan Society for the Promotion of Science (KAKENHI—Grants in-Aid for Scientific Research; Grant Numbers JP22403016, JP25247084, JP26701004, JP26241003, JP16H01772, JP18H03363, JP18H05292, and JP21H03582), the Environment Research and Technology Development Fund (JPMEERF20202003, JPMEERF20232001 and JPMEERF20262002) of the Environmental Restoration and Conservation Agency provided by Ministry of the Environment of Japan, the Arctic Challenge for Sustainability 3 (ArCS-3) (JPMXD1720251001), a grant for the Global Environmental Research Coordination System from Ministry of the Environment of Japan (MLIT2253), and the Ministry of Education, Culture, Sports, Science and Technology (MEXT) Program for the advanced studies of climate change projection (SENTAN) Grant Number JPMXD0722680734.

Author contributions

K.K. designed the research, wrote the manuscript, and prepared the figures. N.O. performed the climate model calculations, generated climate data, and wrote the sections on climate/meteorological changes and methods. T.A. compiled the fossil data and wrote the sections on fossil data, including Figure 1, and the methods. K.K., N.O., and T.A. reviewed and edited the manuscript.

Competing interests

The authors declare no competing interests.

Additional information

Supplementary information The online version contains supplementary material available at https://doi.org/10.------

Correspondence and requests for materials should be addressed to Kunio Kaiho.

Data Availability

All data supporting the findings of this study are available within the paper and its Supplementary Information.

References

1. Alvarez, L. W., Alvarez, W., Asaro, F. & Michel, H. V. Extraterrestrial cause for the Cretaceous-Tertiary extinction. *Science* **208**, 1095–1108 (1980).
2. Hildebrand, A. R. et al. Chicxulub crater: A possible Cretaceous-Tertiary boundary impact crater on the Yucatán Peninsula, Mexico. *Geology* 19, 867–871 (1991).
3. Schulte, P. et al. The Chicxulub asteroid impact and mass extinction at the Cretaceous–Paleogene boundary. *Science* **327**, 1214–1218 (2010).
4. Brusatte, S. L. et al. The extinction of the dinosaurs. *Biol. Rev.* **90**, 628–642 (2015).
5. Font, E., Chen, J., Regelous, M., Regelous, A. & Adatte, T. Volcanic origin of the mercury anomalies at the Cretaceous-Paleogene transition of Bidart, France. *Geology* **50**, 142–146 (2022).
6. Kaiho, K. et al. Dual Hg peaks and isotopic convergence reveal sequential Deccan volcanism and Chicxulub impact at the K–Pg boundary. *Palaeogeogr Palaeoclimatol Palaeoecol*. **695**, 113831 (2026).
7. Robertson, D. S., McKenna, M. C., Toon, O. B., Hope, S. & Lillegraven, J. A. *Survival first hours Cenozoic Geol Soc. Am. Bull*, **116**, 760–768 (2004).
8. Robertson, D. S., Lewis, W. M., Sheehan, P. M. & Toon, O. B. K-Pg extinction: Reevaluation of the heat-fire hypothesis. *J. Geophys. Res. Biogeosci*. **118**, 329–336 (2013).
9. Goldin, T. J. & Melosh, H. J. Self-shielding of thermal radiation by Chicxulub impact ejecta: Firestorm or fizzle? *Geology* **37**, 1135–1138 (2009).
10. Ivanov, B. A. et al. Degassing of sedimentary rocks due to Chicxulub impact: Hydrocode and physical simulations. *Geol. Soc. Am. Spec. Pap*. **307**, 125–139 (1996).
11. Kaiho, K. et al. Global climate change driven by soot at the K-Pg boundary as the cause of the mass extinction. *Sci. Rep.* **6**, 28427 (2016).
12. Senel, C. B. et al. Chicxulub impact winter sustained by fine silicate dust. Nat. Geosci. **16**, 1033–1040 (2023).
13. Kaiho, K. & Oshima, N. The significance of impact-induced hydrocarbon soot aerosols in global climate change and extinctions. *Palaeogegr Palaeoclimatol Plaeoecol*. **678**, 113237 (2025).
14. Rodiouchkina, K. Reduced contribution of sulfur to the mass extinction associated with the Chicxulub impact event. *Nat. Commun.* **16**, 620 (2025).
15. Chiarenza, A. A. et al. Asteroid impact, not volcanism, caused the end-Cretaceous dinosaur extinction. *Proc. Nat. Acad. Sci. USA* 117, 17084–17093 (2020).
16. Sheehan, P. M. & Coorough, P. J. Biotic selectivity during the K/T and Late Ordovician extinction events. *Geol. Soc. Am. Spec. Pap*. **307**, 477–489 (1996).
17. Wiest, L. A., Lukens, W. E., Peppe, D. J., Driese, S. G. & Tubbs, J. Terrestrial evidence for the Lilliput effect across the Cretaceous-Paleogene (K-Pg) boundary. *Palaeogegr Palaeoclimatol Plaeoecol*. **491**, 161–169 (2018).
18. Fastovsky, D. E. & Bercovici, A. The Hell Creek Formation and its contribution to the Cretaceous-Paleogene extinction: A short primer. *Cretac. Res.* **57**, 368–390 (2016).
19. Feduccia, A. Avian extinction at the end of the Cretaceous: Assessing the magnitude and subsequent explosive radiation. *Cretac. Res.* **50**, 1–15 (2014).
20. Field, D. J. et al. Early evolution of modern birds structured by global forest collapse at the end-Cretaceous mass extinction. *Curr. Biol.* **28**, 1825–1831 (2018).
21. Wilf, P. & Johnson, K. R. Land plant extinction at the end of the Cretaceous: a quantitative analysis of the North Dakota megafloral record. *Paleobiology* **30**, 347–368 (2004).

22. Worthy, T. H., Degrange, F. J., Handley, W. D. & Lee, M. S. Y. The evolution of giant flightless birds and novel phylogenetic relationships for extinct fowl (Aves, Galloanseres). R. Soc. Open Sci. **4**, 170975 (2017).
23. Longrich, N. R., Scriberas, J. & Wills, M. A. Severe extinction and rapid recovery of mammals across the Cretaceous–Palaeogene boundary, and the effects of rarity on patterns of extinction and recovery. *J. Evol. Biol.* **29**, 1495–1512 (2016).
24. Lehmkuhl, J. Determining size and dispersion of minimum viable populations for land management planning and species conservation. *Environ. Manage.* **8**, 167–176 (1984).
25. Thomas, C. D. What do real population dynamics tell us about minimum viable population sizes? *Conserv. Biol.* **4**, 324–327 (1990).
26. Gatesy, S. M. & Dial, K. P. From frond to fan: Archaeopteryx and the evolution of short-tailed birds. Evolution. *Int. J. Org. Evol.* **50**, 2037–2048 (1996).
27. Clarke, J. A., Zhou, Z. & Zhang, F. Insight into the evolution of avian flight from a new clade of Early Cretaceous Ornithurines from China and the morphology of *Yixianornis grabaui*. *J. Anat.* **208**, 287–308 (2006).
28. Lee, S. et al. A New Alvarezsaurid Dinosaur from the Nemegt Formation of Mongolia. Sci. Rep. **9**, 15493 (2019).
29. Ishida, H., Kaiho, K. & Asano, S. Effects of a large asteroid impact on ultra-violet radiation in the Atmosphere. *Geophys. Res. Lett.* **34**, L23805 (2007).
30. Hosseini, S. H. R., Kaiho, K. & Takayama, K. Response of ocean bottom dwellers exposed to underwater shock waves. *Shock Waves*. **26**, 69–74 (2016).
31. Burgener, L., Hyland, E., Reich, B. J. & Scotese, C. Cretaceous climates: Mapping paleo- Köppen climatic zones using a Bayesian statistical analysis of lithologic, paleontologic, and geochemical proxies. *Palaeogeogr Palaeoclimatol Palaeoecol*. **613**, 111373 (2023).
32. Kaiho, K. & Oshima, N. Site of asteroid impact changed the history of life on Earth: the low probability of mass extinction. *Sci. Rep.* **7**, 14855 (2017).
33. Ohno, S. et al. Production of sulphate-rich vapour during the Chicxulub impact and implications for ocean acidification. Nat. Geosci. **7**, 279–282 (2014).
34. Foley, J. A. Net primary productivity in the terrestrial biosphere: The application of a global model. J. Geophys. Res. **99**, 20,773 – 20,783 (1994).
35. Altangerel, P., Norell, M. A., Chiappe, L. M. & Clark, J. M. Flightless bird from the Cretaceous of Mongolia. Nature **362**, 623–626 (1993).
36. Baldwin, J. W. & Myers, J. A. Avian dispersal ability shapes species–area relationships on islands worldwide. *Ecol. Lett.* **27**, e70020. https://doi.org/10.1111/ele.70020 (2024).
37. Franklin, I. R. Evolutionary changes in small populations. In M. E. Soulé & B. A. Wilcox (Eds.), *Conservation Biology: An evolutionary-ecological perspective* (pp. 135–149) (1980).
38. Traill, L. W., Bradshaw, C. J. & Brook, B. W. Beyond the Fray: Protecting species from extinction. *Trends Ecol. Evol.* **22**, 106–112 (2007).
39. Flather, C. H. et al. Minimum viable population size: not a magic number. *rends Ecol. Evol.* **26**, 307–316 (2011).
40. Bardeen, C. G., Garcia, R. R., Toon, O. B. & Conley, A. J. On transient climate change at the Cretaceous–Paleogene boundary due to atmospheric soot injections. *Proc. Nat. Acad. Sci.* 114, E7415–E7424 (2017).
41. Brodkorb, P. Birds from the Upper Cretaceous of Wyoming. *Contrib. Geol.* **2**, 55–59 (1963).
42. Olson, S. L. & Parris, D. C. The Cretaceous birds of New Jersey. *Smithson. Contrib. Paleobiol.* **63**, 1–22 (1987).
43. Hope, S. The Mesozoic radiation of Neornithes. In: (eds Chiappe, L. M. & Witmer, L. M.) Mesozoic Birds: Above the Heads of Dinosaurs. University of California Press, Berkeley, 339–388 (2002).
44. Dyke, G. J. & Van Tuinen, M. The evolutionary radiation of modern birds (Neornithes): Reconciling molecules, morphology and the fossil record. *Zoological J. Linn. Soc.* **141**, 153–177 (2004).
45. Clarke, J., Tambussi, C., Noriega, J., Erickson, G. M. & Ketcham, R. A. Definitive fossil evidence for the extant avian radiation in the Cretaceous. *Nature* **433**, 305–308 (2005).
46. O'Connor, J. K., Gao, K. Q. & Chiappe, L. M. A new ornithuromorph (Aves: Ornithothoraces) bird from the Jehol Group indicative of higher-level diversity. *J. Vertebrate Paleontol.* **30**, 311–321 (2010).
47. Longrich, M. R., Tokaryk, T. & Field, D. J. Mass extinction of birds at the Cretaceous-Paleogene (K-Pg) boundary. *Proc. Nat. Acad. Sci. USA* 108, 15253–15257 (2011).
48. Field, D. J. et al. Late Cretaceous Neornithine from Europe Illuminates the Origins of Crown Birds. *Nature* **579**, 397–401 (2020).
49. Müller, R. D. et al. GPlates: Building a Virtual Earth through deep time. *Geochem. Geophys. Geosyst.* **19**, 2243–2261 (2018).
50. QGIS Development Team. QGIS Geographic Information System. *Open. Source Geospatial Foundation Project* (2025). https://qgis.org
51. Scotese, C. R. Some Thoughts on Global Climate Change: The Transition for Icehouse to Hothouse Conditions. PALEOMAP Project. (2016). https://www.researchgate.net/publication/275277369

52. Yukimoto, S. et al. A new global climate model of the Meteorological Research Institute: MRI-CGCM3 -Model description and basic performance. *J. Meteor. Soc. Japan*. **90A**, 23–64 (2012).
53. Saito, T., Kaiho, K., Abe, A., Katayama, M. & Takayama, K. Hypervelocity impact of asteroid/comet on the oceanic crust of the earth. *Int. J. Impact Eng.* **35**, 1770–1777 (2008).
54. Yukimoto, S. et al. The Meteorological Research Institute Earth System Model version 2.0, MRI-ESM2.0: Description and basic evaluation of the physical component. *J. Meteor. Soc. Japan*. **97**, 931–965 (2019).
55. Oshima, N. et al. Global and Arctic effective radiative forcing of anthropogenic gases and aerosols in MRI-ESM2.0. *Prog Earth Planet. Sci.* **7**, 38 (2020).
56. Thomason, L. W. et al. A global space-based stratospheric aerosol climatology: 1979–2016. *Earth Sys Sci. Data*. **10**, 469–492 (2018).
57. Lozano-Parra, J., Schnabel, S. & Pulido, M. Effects of soil moisture and vegetation cover on biomass growth in water-limited environments. *Land Degradation Development*. **29**, 4405–4414 (2018).
58. Lozano-Parra, J., Pulido, M., Lozano-Fondón, C. & Schnabel, S. How do soil moisture and vegetation covers influence soil temperature in drylands of Mediterranean regions? *Water* 10, 1747 (2018).
59. De Niem, D., Kührt, E. & Motschmann, U. Ejecta range: A simulation study of terrestrial impacts. *Planet. Space Sci.* **55**, 900–914 (2007).
60. Pope, K. O., Baines, K. H., Ocampo, A. C. & Ivanov, B. A. Energy, volatile production, and climatic effects of the Chicxulub Cretaceous/Tertiary impact. *J Geophys. Res* **102**, (1997). 21,645 – 21,664.
61. Kaiho, K. Role of volcanism and impact heating in mass extinction climate shifts. *Sci Rep.* **14**, 9946 (2024)). .
62. Lyons, S. L. et al. Organic matter from the Chicxulub crater exacerbated the K-Pg impact winter. *Proc. Nat. Acad. Sci. USA* 117, 25327 – 25334. (2020).
63. Wolbach, W. S., Gilmour, I. & Anders, E. Major wildfires at the Cretaceous/Tertiary boundary. *Geol. Soc. Am. Spec. Pap*. **247**, 391–400 (1990).
64. Emery, K. O. Relict sediments on continental shelves of world. *Am. Assoc. Petrol. Geol. (AAPG) Bull.* **52**, 445–464 (1968).
65. Yu et al. Black carbon lofts wildfire smoke high into the stratosphere to form a persistent plume. *Science* **365**, 587–590 (2019).
66. Yu et al. Persistent stratospheric warming due to 2019–2020 Australian wildfire PyroCb emissions. *Geophys. Res. Lett.* **48**, e2021GL092609 (2019).
67. Catharina, A. S. et al. Timing and causes of forest fire at the K–Pg boundary. *Sci. Rep.* **12**, 13006 (2022).
68. Mitchell, M. J. et al. Sulfur budget of a forested catchment in the Adirondack Mountains of New York. *Water Air Soil Pollut.* **130**, 691–696 (2001).
69. Zhang, Y. et al. An updated global mercury budget from a coupled atmosphere-land-ocean model: 40% more re-emissions buffer the effect of primary emission reductions. *One Earth*. **6**, 316–325 (2023).
70. Vellekoop, J. et al. Evidence for Cretaceous-Paleogene boundary bolide impact winter conditions from New Jersey, USA. *Geology* **44**, 619–622 (2016).
71. Downs, C. T., Greaver, C. & Taylor, R. Body temperature and basking behaviour of Nile crocodiles. J. Thermal Biol. 33, 185–192 (2008). (2025).
72. Pierazzo, E., Hahmann, A. N. & Sloan, L. C. Chicxulub and climate: radiative perturbations of impact-produced S-bearing gases. *Astrobiology* **3**, 99–118 (2003).
73. Badjukov, D. D., Dikov, Y. P., Petrova, T. L. & Pershin, S. V. Shock behavior of calcite, anhydrite. and gypsum (Abstr). *Lunar Planet. Sci. Conf. XXVI* 63–64. (1995). Lunar Planet. Inst. Houston. TX.
74. Ivanov, B. A. et al. Degassing of sedimentary rocks due to Chicxulub impact: Hydrocode and physical simulations. *Geol. Soc. Am. Spec. Pap*. **307**, 125–139 (1996).
75. Judd, E. J. et al. A 485-million-year history of Earth's surface temperature. *Science* **385**, 1316 (2024).
76. Upchurch, G. R., Jr, Otto-Bliesner, B. L. & Scotese, C. Vegetation–atmosphere interactions and their role in global warming during the latest Cretaceous. *Phil Trans. R Soc. Lond. B*. **353**, 97–112 (1998).
77. Osaki, S., Uchida, M. & Nakatsubo, T. Thermal germination characteristics of three High Arctic plants: Implications for their response to climate warming. *Polar Sci.* **39**, 101045 (2024).
78. Lieth, H. Modeling the primary productivity of the world, in Primary Productivity of the Biosphere, (eds Leith, H. & Whittaker, R. H.) 237–263 (Springer-, New York., (1975).
79. Miyoshi, C., Sodeyama, S. & Genkai-Kato, M. Relationships between energy intake and body mass in captive animals. *Anim. Behav. Manage.* **52**, 98–105 (2016).

Table

Table 1. Number of individuals in a species in a refuge (western northern Africa) for bird after the K-Pg meteoroid impact (a) and abundance (number of individuals) of each animal group in a typical survival area (b). Body weight of non-avian dinosaurs and birds are described in the Results section. F = 0.13W x 365 (for one individual). 0.13: Rate of food weight for bird weight a day[64]. Number of species is based on avian high dispersal ability and non-avian dinosaur low dispersal ability shaping species-area relationships on islands worldwide in Baldwin et al.[36]. R_S: from number of species under high NPP, 6 and 33, calculated from ln1.8 to ln3.5 in log (Species) in Figure 5 of Baldwin et al.[36] except for the Palearctic realm. The post-impact refugia case is low NPP. Therefore, we used rate of species (R_S) for the post-impact refugia. R_A: calculated from avian abundance and species richness in modern temperate grasslands [78] using rate of species (R_S) (Supplementary Table 9). A = (0.2 x 2 x 10^{11} x 0.001 x 0.045 x R_A)/F. 0.2: NPP (0.11–0.3 [kg C m^{-2} yr^{-1}]) in average for small refugia for birds. 2 x 10^{11}: inhabitable area (m^2, western northern Africa). 0.001: Rate of animal and plant in weight. 0.1: Rate of terrestrial vertebrates (0.009 Gt C) in terrestrial vertebrates and terrestrial arthropods (0.2 Gt C) except for soil arthropods in weight[77, 79]. (0.2 x 2 x 10^{11} x 0.001): Food (Kg yr^{-1}) for terrestrial animals. (0.2 x 2 x 10^{11} x 0.001 x 0.045): Food (Kg yr^{-1}) for terrestrial vertebrate (tetrapods). *when number of species of non-avian dinosaurs and birds are one and five, respectively, under low NPP.

a	Body	Food					
	weight	/year	Number of	Rate of	Rate of		Average	
	(Kg)	(Kg)	species	species	abundance	Abundance	abundance	
Dinosaur group	(W)	(F)	high NPP	(R_S)	(R_A)	(A)	/species*	Results
Small non-avian dinosaurs	3	142.4	6	0.15	0.04	1,000	1,000	Extinction
(low dispersal ability)	20	949				200	200	Extinction
Surviving birds	0.4	19	33	0.85	1	$200*10^3$	$40*10^3$	Survival
(high dispersal ability)	3	142.4				$30*10^3$	$6*10^3$	Survival

b	Typical	Dinosauria	Aves	Crocodylomorpha	Mammalia
A refuge area of	survival area	(non-avian)			
Dinosauria (non-avian)	SW Asia island	200–1,000	30,000–200,000	0	Abundant
Aves	NW Africa	200–1,000	30,000–200,000	0	Abundant
Crocodylomorpha	Maritime Continent	0	0	Abundant	Abundant
Mammalia	Africa	200–1,000	30,000–200,000	rare	Abundant

Figures

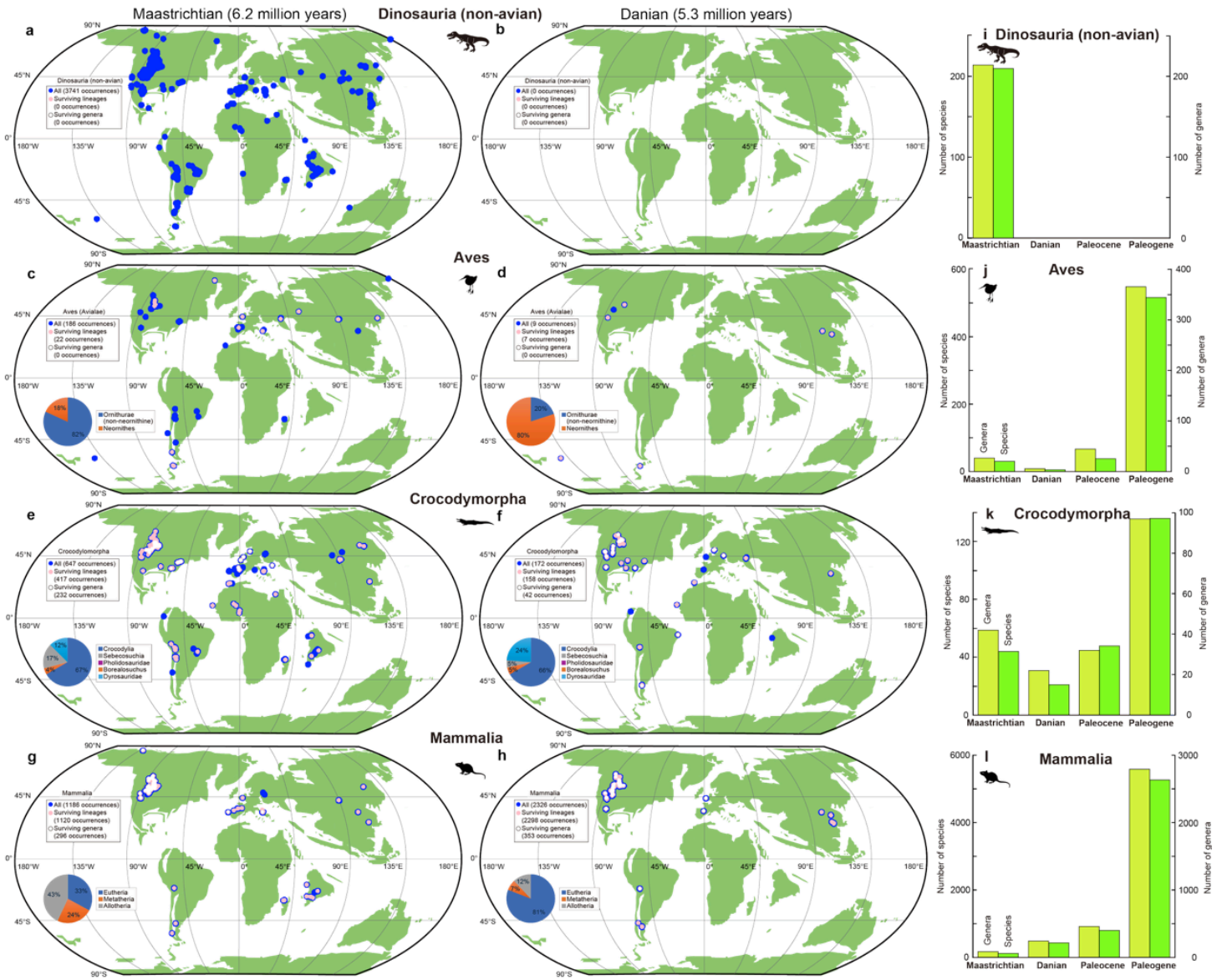


Figure 1

Fossil distribution (a–h) and number of genera and species (i–l) in each age for non-avian dinosaurs, birds, crocodilians, and mammals. a, **b**, Non-avian dinosaurs. **c**, **d** Birds (Aves). **e**, **f**, Crocodilians. **g**, **h**, Mammals. **a**, **c**, **e**, **g**, Maastrichtian. **b**, **d**, **f**, **h**, The first to third years after the impact. Red arrows in **d** and **f** indicate survival migration across the impact event. Stars in **b** and **d** mark the location of the Chicxulub impact. Base maps at 66 Ma are from Scotese[51].

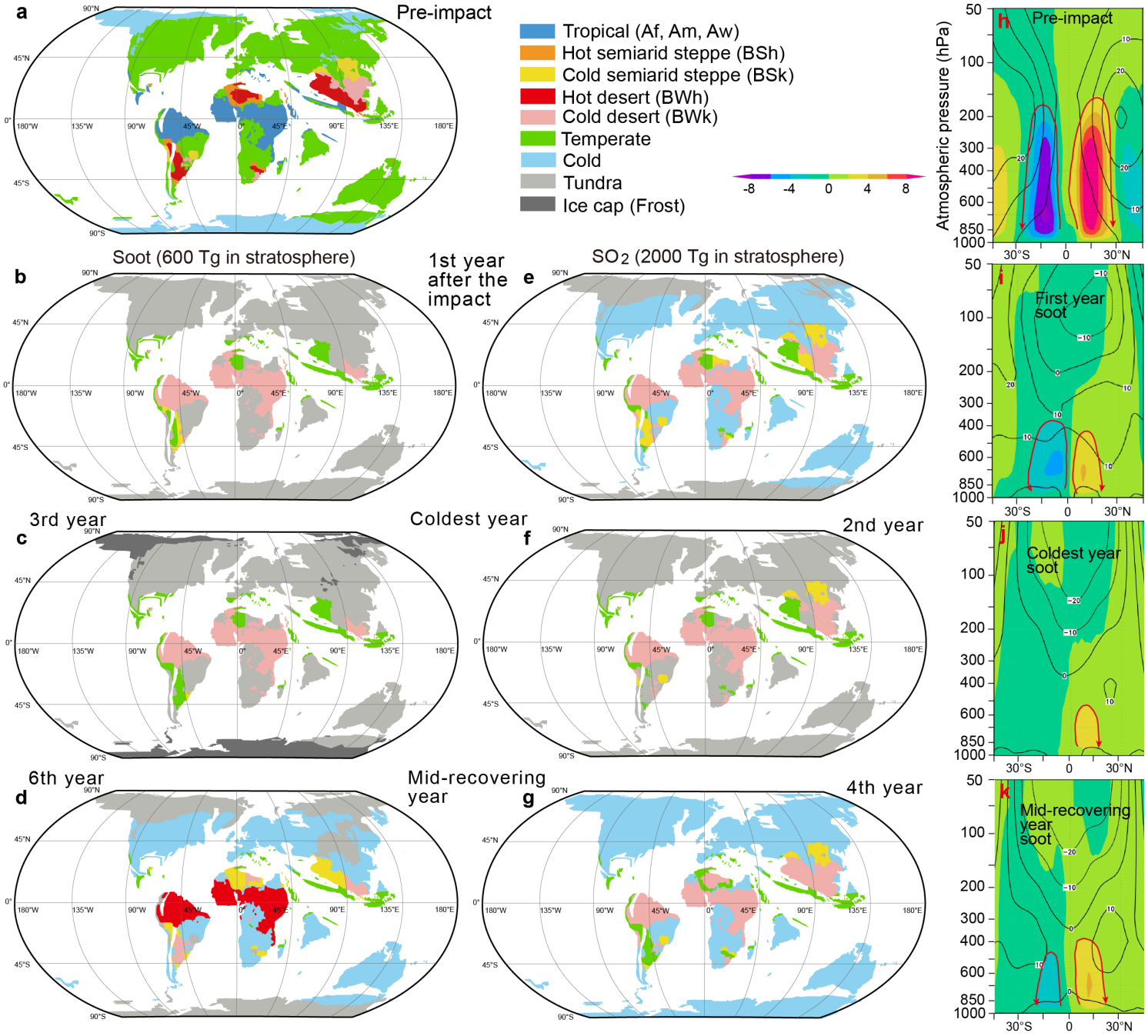


Figure 2

Köppen climate classification maps and vertical distributions of zonal mean atmospheric circulation illustrating the results from the Chicxulub impact at 66 million years ago. The pre-impact map formed based on a climate classification map of Burgener et al.[31]. **b**–**d**, the soot case (stronger-cooling impact case). **e**–**g**, the SO_2 case. These maps are formed by applying the climate zone change patterns between pre-impact and post-impact in modern Earth (Supplementary Tables 4 and 5) to the Maastrichtian climate classification map of Burgener et al.[31]. Oceanic tropical and warm temperate as shown in Supplementary Figure 3b, c, f, g, j. The change patterns are based on 0–500 m elevation areas in Supplementary Figure 2. The base maps at 66 million years ago are from Scotese[51]. **h**–**k**, zonal mean atmospheric circulation. See also Supplementary Tables 4 and 5.

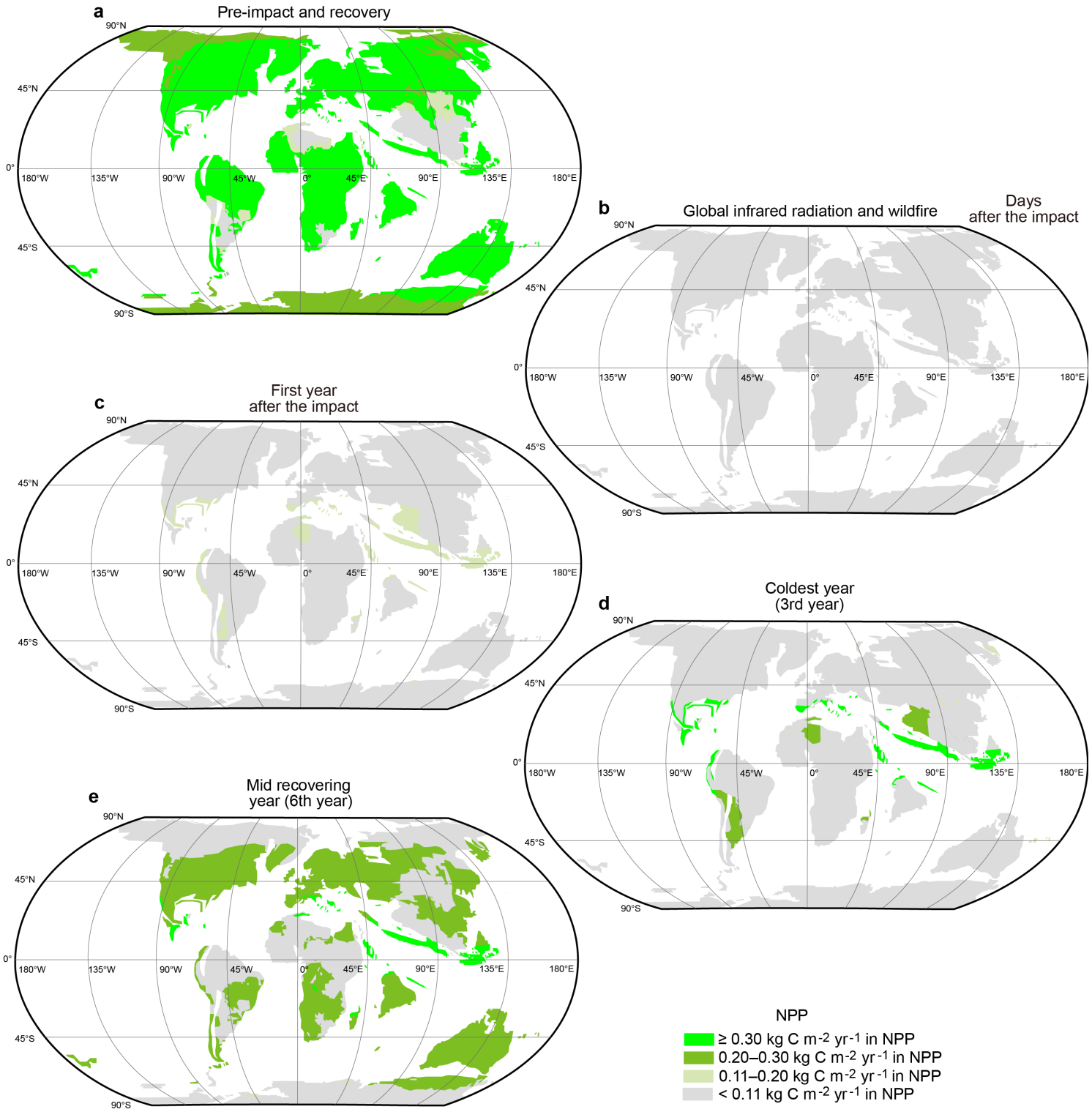


Figure 3

Modelling estimation of global distribution of terrestrial net primary productivity (NPP) before and after the Chicxulub impact. Vegetation based on net primary productivity calculated using temperature, precipitation, and sunlight [see Methods]). Diversity of birds based on net primary productivity. The base maps at 66 million years ago are from Scotese[51].

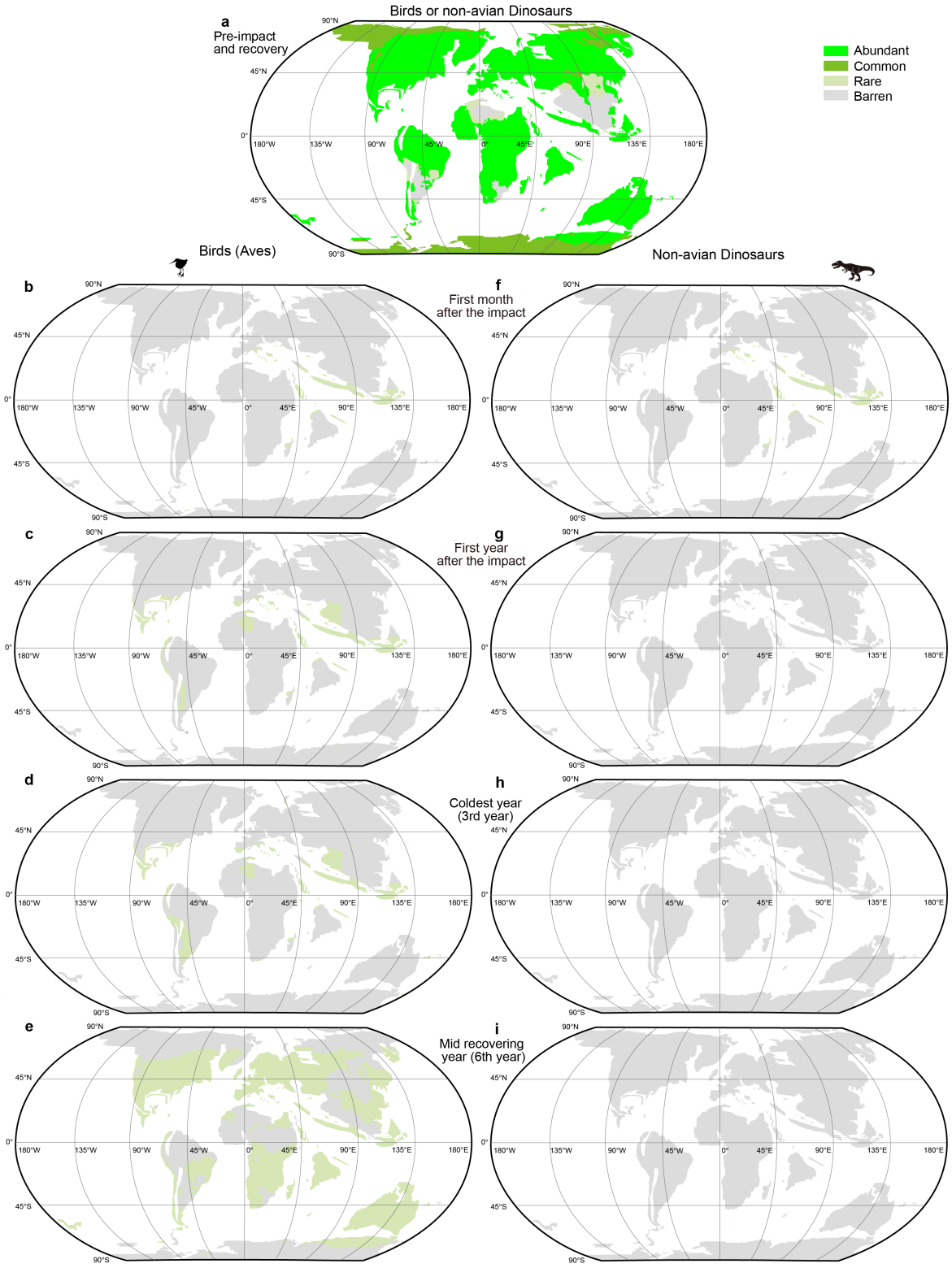


Figure 4

Modelling estimation of inhabitable areas of birds and non-avian dinosaurs before and after the Chicxulub impact (colored areas). b–d, Diversity of birds based on net primary productivity (Fig. 4) after the impact. **e–g**, Diversity of dinosaurs (excluding ground-dwelling birds) based on net primary productivity (Fig. 4). The base maps at 66 million years ago are from Scotese[51].

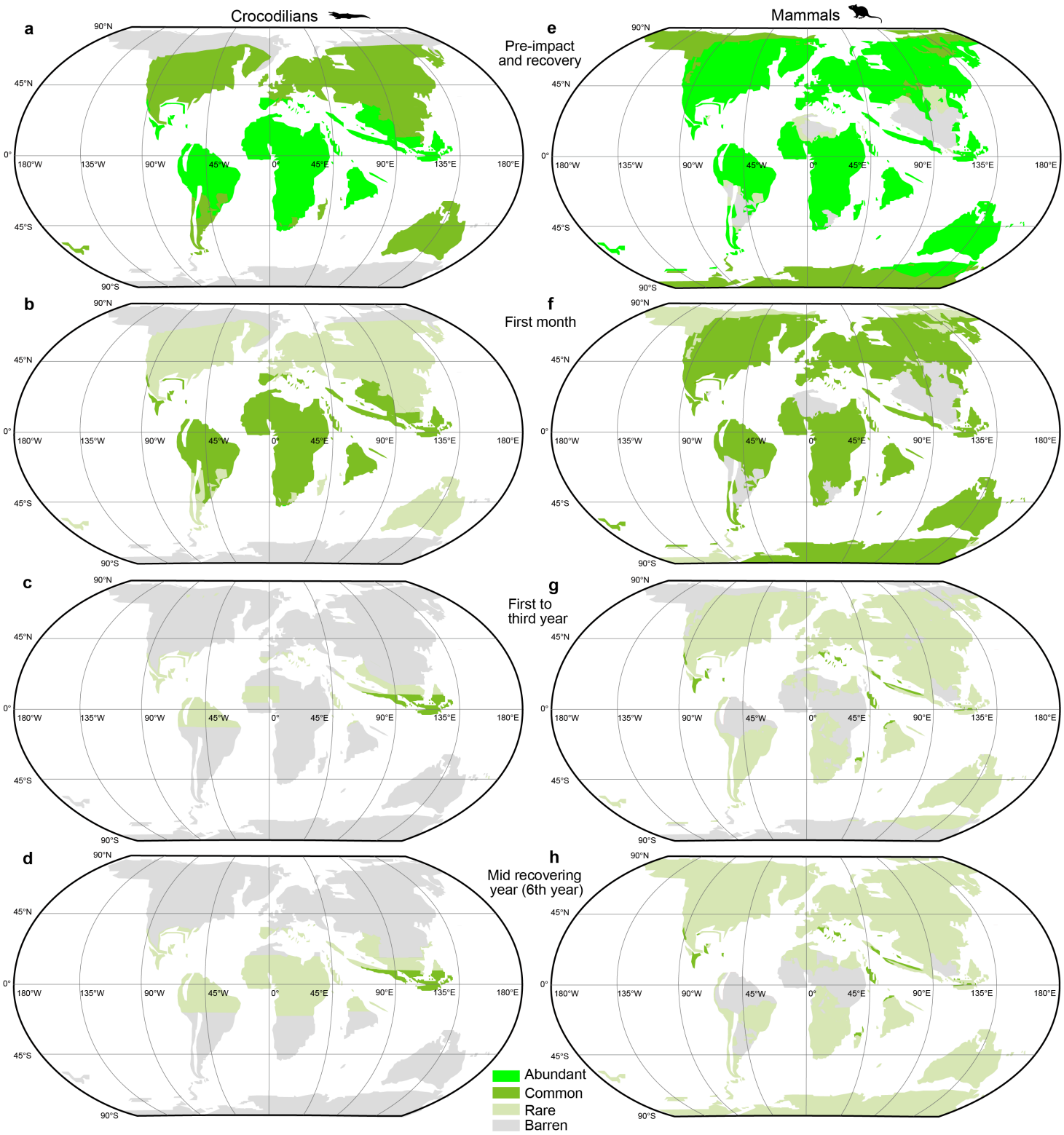


Figure 5

Modelling estimation of inhabitable areas of mammals and crocodilians before and after the Chicxulub impact (colored areas) with their fossil occurrences in the Maastrichtian and Danian ages (dots). a–**d**, Diversity of crocodilians based on surface temperature (Burgener et al.[31], Supplementary Tables 4, 6, 8, 13, 14). **e**–**h**, Diversity of mammals based on climate classification map (Fig. 3). The base maps at 66 million years ago are from Scotese[51].

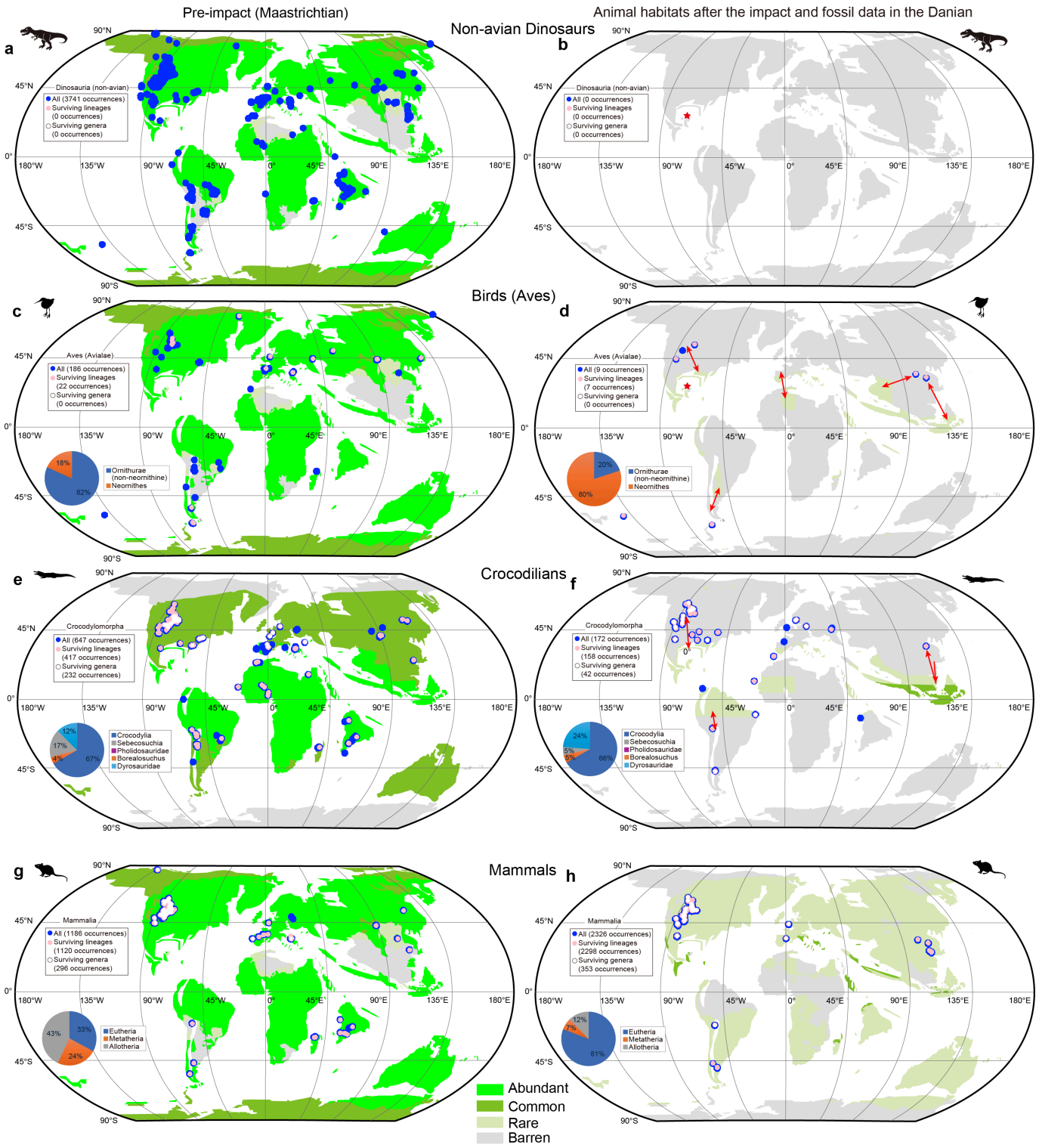


Figure 6

Minimum inhabitable areas for non-avian dinosaurs, birds, crocodylomorphs and mammals during the Maastrichtian and the first to third years after the impact, including survival migration over the subsequent 15 years or longer. a, **b**, Non-avian dinosaurs. **c**, **d** Birds (Aves). **e**, **f**, Crocodilians. **g**, **h**, Mammals. **a**, **c**, **e**, **g**, Maastrichtian. **b**, **d**, **f**, **h**, The first to third years after the impact. Red arrows in **d** and **f** indicate survival migration across the impact event. Stars in **b** and **d** mark the location of the Chicxulub impact. Base maps at 66 Ma are from Scotese[51].

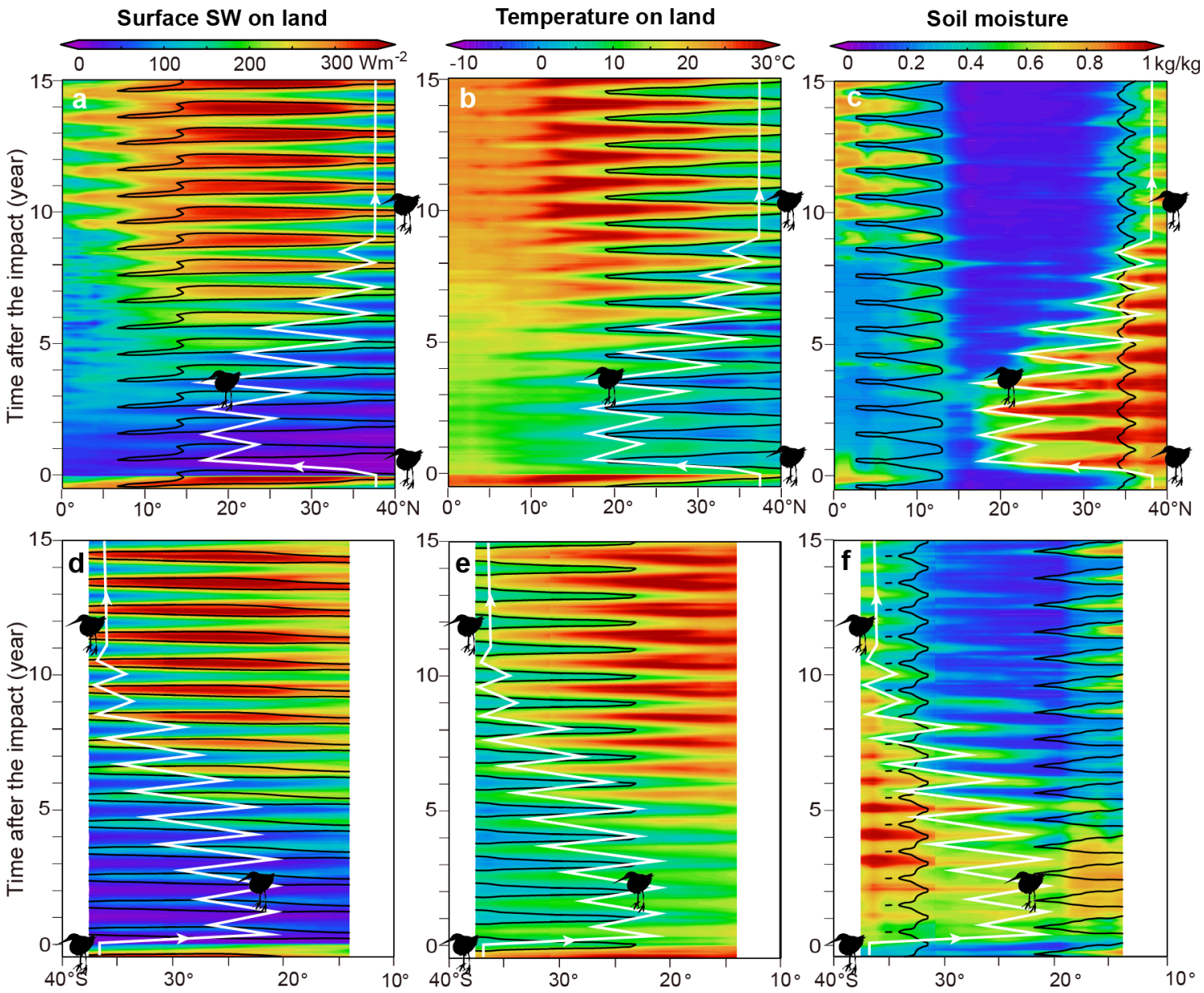


Figure 7

Estimated migration routes of ground-dwelling birds (white line with arrows) over southern Europe – northwestern Africa region and Australia – Indonesia region in the stronger-cooling impact case (soot). **a**–**c**, southern Europe – northwestern Africa region. These data are averaged in longitudinally between 10°W and 10°E on the modern Earth. (**d**–**f**) Australia – Indonesia region. These data are averaged in longitudinally between 115°E and 130°E on the modern Earth. **a**, **d**, downward shortwave (SW) radiation at the surface on land. Black curves indicate 1 mm/day in the pre-impact case (the control experiment). **b**, **e**, surface air temperatures on land. Black curves indicate 15°C in the pre-impact case (the control experiment). **c**, **f**, degree of soil moisture saturation averaged for a depth of 0–5 cm (kg kg^{-1}). Black curves indicate 0.3 kg/kg and 3 kg/m^2 in the pre-impact case (the control experiment).

Supplementary Files

This is a list of supplementary files associated with this preprint. Click to download.

- KaihoSurvivalSI24.docx